Miner Petrol (2014) 108:49–69
DOI 10.1007/s00710-013-0277-3

ORIGINAL PAPER

Geochemical make-up of oceanic peridotites from NW Turkey and the multi-stage melting history of the Tethyan upper mantle

İbrahim Uysal · A. Dündar Şen · E. Yalçın Ersoy · Yildirim Dilek · Samet Saka · Federica Zaccarini · Monica Escayola · Orhan Karslı

Received: 1 July 2012 / Accepted: 13 February 2013 / Published online: 14 March 2013

Abstract We present the whole-rock and the mineral chemical data for upper mantle peridotites from the Harmancık region in NW Turkey and discuss their petrogenetic–tectonic origin. These peridotites are part of a Tethyan ophiolite belt occurring along the İzmir-Ankara-Ercincan suture zone in northern Turkey, and include depleted lherzolites and refractory harzburgites. The Al_2O_3 contents in orthopyroxene and clinopyroxene from the depleted lherzolite are high, and the Cr-number in the coexisting spinel is low falling within the abyssal field. However, the orthopyroxene and clinopyroxene in the harzburgites have lower Al_2O_3 contents for a given Cr-number of spinel, and plot within the lower end of the abyssal field. The whole-rock geochemical and the mineral chemistry data imply that the Harmancık peridotites formed by different degrees of partial melting (~%10–27) of the mantle. The depleted lherzolite samples have higher MREE and HREE abundances than the harzburgitic peridotites, showing convex-downward patterns. These peridotites represent up to ~16 % melting residue that formed during the initial seafloor spreading stage of the Northern Neotethys. On the other hand, the more refractory harzburgites represent residues after ~4–11 % hydrous partial melting of the previously depleted MOR mantle, which was metasomatized by slab-derived fluids during the early stages of subduction. The Harmancık peridotites, hence, represent the fragments of upper mantle rocks that formed during different stages of the tectonic evolution of the Tethyan oceanic lithosphere in Northern Neotethys. We infer that the multi-stage melting history of the Harmancık peridotites reflect the geochemically heterogeneous character of the Tethyan oceanic lithosphere currently exposed along the İzmir-Ankara-Erzincan suture zone.

Editorial handling: M. Fiorentini

İ. Uysal (✉) · S. Saka
Department of Geological Engineering, Karadeniz Technical University, 61080 Trabzon, Turkey
e-mail: iuysal@ktu.edu.tr

İ. Uysal
e-mail: uysal.ibrahim@gmail.com

A. D. Şen
Department of Geological Engineering, Gümüshane University, 29000 Gümüshane, Turkey

E. Y. Ersoy
Department of Geological Engineering, Dokuz Eylül University, 35000 İzmir, Turkey

Y. Dilek
Department of Geology and Env. Earth Science, Miami University, Oxford, OH 45056, USA

F. Zaccarini
Department of Applied Geological Sciences & Geophysics, Montanuniversitaet, 8700 Leoben, Austria

M. Escayola
Facultad de Ciencias Exactas y Naturales-Universidad de Buenos Aires, Pabellón II-Oficina 102-Nuñez-C1428ZAA, Ciudad Autónoma de Buenos Aires, Argentina

O. Karslı
Department of Geological Engineering, Recep Tayyip Erdoğan University, 53000 Rize, Turkey

Introduction

Abyssal peridotites are interpreted to be residual products of variable degrees of adiabatic mantle melting resulting from decompression and melt extraction processes beneath the

mid-ocean spreading centers (e.g. Niu et al. 1997; Hellebrand et al. 2002; Niu 2004). Their geochemical signatures may be well preserved in the bulk-rock and mineral compositions despite extensive serpentinization and seafloor hydrothermal alteration. Recent studies of abyssal peridotites have shown a compositional heterogeneity of the lithospheric mantle that is caused by various geochemical and petrological processes (Kelemen et al. 1997; Niu et al. 1997; Piccardo et al. 2007; Rampone et al. 2008; Uysal et al. 2007). The compositions of abyssal peridotites provide, therefore, important constraints for better understanding the melting and melt extraction processes beneath seafloor spreading centers through time.

Mineralogical and chemical characteristics of dismembered peridotites in ophiolites are also a significant source of information about the melt evolution and dynamics of the upper mantle in different tectonic settings (e.g. Parkinson and Pearce 1998; Flower and Dilek 2003; Uysal et al. 2007; 2012; Seyler et al. 2007; Choi et al. 2008). Anhydrous mafic silicates and spinels show a wide range of chemical compositions largely resulting from primary melting and mixing processes that occurred in the ancient upper mantle. Primary spinel in particular is an important petrogenetic indicator whose chemical composition largely depends on the degree of partial melting, melt-peridotite interactions and physical conditions (i.e. pressure, temperature and oxygen fugacity) of partial melting of the host peridotites (e.g. Dick and Bullen 1984; Arai 1994; Zhou and Robinson 1997; Parkinson and Pearce 1998; Choi et al. 2008). Generally, those peridotite massifs containing economically important chromite deposits are interpreted to be supra-subduction zone type, whereas chromitite-free peridotites are attributed to MOR-type abyssal in origin (Edwards et al. 2000).

Most Tethyan ophiolites occurring in the eastern Mediterranean region are interpreted as fragments of SSZ–generated oceanic lithosphere (Pearce et al. 1984; Robertson 1994; Dilek et al. 1999; Parlak et al. 2002; Dilek et al. 2007; Dilek and Flower 2003; Dilek and Furnes 2009) based mainly on the geochemical features of their upper crustal units. Since SSZ ophiolites were in general produced during the latest closing stages of ancient ocean basins (Dilek and Furnes 2011), the Tethyan ophiolites with SSZ characteristics are widely interpreted to have formed in incipient arc–forearc settings shortly before their emplacement on continental margins. These processes may have resulted in limited compositions and degrees of melting of upper mantle peridotites in SSZ tectonic settings, and hence in relatively simple depletion and refertilization events in their evolutionary history. However, recent studies of many Tethyan ophiolites have shown that these fragments of ancient oceanic lithosphere display significant structural and compositional heterogeneities, and their peridotites show chemical fingerprint of various and multiple episodes of melting, melt extraction, and melt–mantle interaction in a more protracted evolutionary history than previously thought (Batanova and Sobolev 2000; Uysal et al. 2007, 2012; Aldanmaz et al. 2009; Dilek and Furnes 2009; Dilek and Morishita 2009; Dilek and Thy 2009; Pearce and Robinson 2010; Morishita et al. 2011a). These findings suggest that the Tethyan ophiolites, particularly their upper mantle components, have a record of a complex magmatic, geochemical and tectonic evolution, spanning different geodynamic settings within the same ocean basin. This inference has in turn significant implications for paleogeographic reconstructions of paleo-oceans, which are based largely on ophiolite ages and affinities.

Here, we present new bulk-rock and mineral chemical data from a suite of representative upper mantle peridotites from the Harmancık area, occurring along the İzmir-Ankara-Erzincan suture zone (IAESZ) in NW Turkey, and discuss their petrogenesis reflecting multiple depletion and enrichment events during their evolution in the northern branch of Neotethys. We think that this evolutionary path of the Harmancık peridotites is a common phenomenon for the tectonomagmatic development of the other ophiolites in the Tethyan realm and in the SW Pacific Ocean.

Regional geology

Tethyan ophiolites in Anatolia occur in several ~ E-W-trending belts, which are separated by a series of Gondwana-derived continental fragments (Dilek and Moores 1990; Robertson 1994). Most of the Tethyan ophiolites in the region have SSZ affinities (Dilek and Furnes 2009). These ophiolite belts mark the ancient suture zones, and together with the locally exposed high-pressure blueschist occurrences, provide strong evidence for the polarity of ancient subduction zones and related trench rollback systems (Okay and Kelley 1994; Dilek and Whitney 1997; Rolland et al. 2009). The IAESZ in northern Turkey occurs between the Skarya Zone (continent) to the north and the Anatolide-Tauride continental block to the south (Fig. 1a), and include a serpentinite-matrix mélange, high-P blueschist rocks, greenschist to amphibolite grade mafic rock units, seamount fragments, and relatively intact ophiolite blocks, which are locally extensive and well-preserved (Tankut et al. 1998; Sherlock et al. 1999; Dilek and Thy 2006). The south-directed transport direction of imbricate thrust faults, the generally north-dipping tectonic fabric elements, and the southward ophiolite and blueschist emplacement directions within the IAESZ collectively suggest a north-dipping subduction polarity within the Northern Neotethys during much of the Mesozoic.

The Harmancık peridotites occur tectonically above the Tavşanlı zone along the IAESZ in NW Turkey (Fig. 1a). The Tavşanlı zone, more than 250 km long and 40 km wide, is a

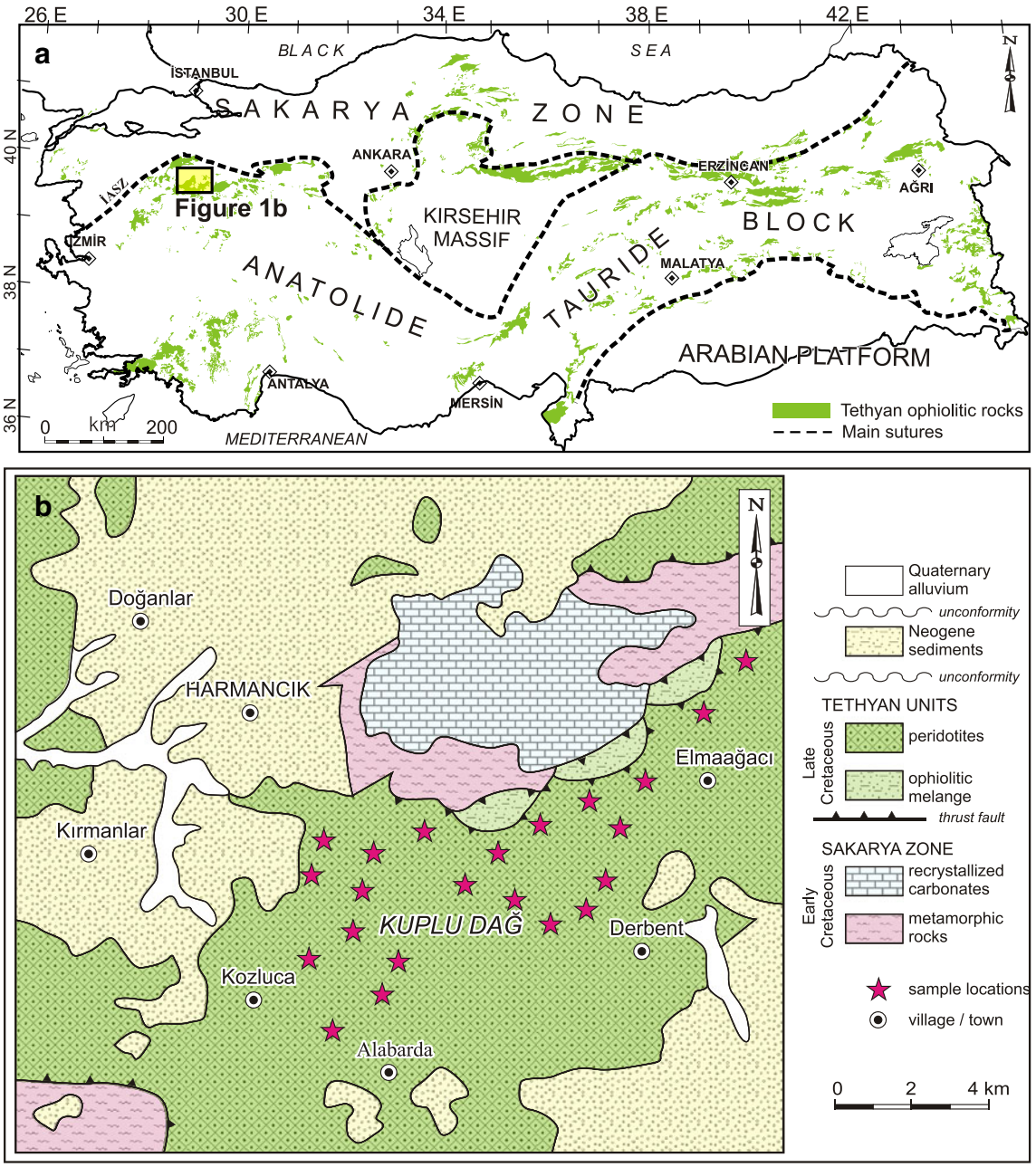

Fig. 1 **a** Distribution of main ophiolite occurrences and suture zones in Turkey, **b** Simplified geological map of the Harmancık area, Bursa, in NW Turkey (modified from Manav et al. 2004) showing the locations of the sampled peridotites

HP-LT metamorphic belt that formed by the subduction and southward accretion of the Neotethyan oceanic lithosphere and the passive continental margins of the Anatolide-Tauride block (e.g. Okay 1986; Sherlock et al. 1999; Droop et al. 2005; Altunkaynak and Dilek 2006; Dilek and Altunkaynak 2007). The Tavşanlı zone consists of a continental micaschist-marble sequence, (lawsonite-blueschist facies) and an oceanic accretionary complex, which is commonly referred to as an ophiolitic mélange. This complex includes blueschist-facies metamorphic rocks and a peridotitic massif containing local garnet-bearing amphibolite at its base (e.g. Okay 1986; Sherlock et al. 1999; Droop et al. 2005; Topuz et al. 2006).

The Harmancık peridotites were emplaced onto the Anatolide-Tauride continental margin during the late Cretaceous (e.g. Özkoçak 1969; Manav et al. 2004). The basement rocks in the area consist of Paleozoic metamorphic rocks that are composed of blueschists and recrystallized carbonates. These are tectonically overlain by thick slabs of peridotites (e.g. Okay 1980; Okay and Kelley 1994; Sherlock et al. 1999) (Fig. 1b). The Harmancık peridotites are unconformably overlain by the Neogene sedimentary units, mainly consisting of

basal conglomerates and coarse-grained sandstones with coal layers deposited in a lacustrine environment.

Analytical methods

Twenty-two peridotite samples collected from the upper mantle units occurring in the Harmancık area of northwestern Turkey (Fig. 1b) were analyzed for their major oxide and loss on ignition (LOI) concentrations by X-ray fluorescence in the commercial laboratory of ACME (Canada). Trace and rare earth element (REE) analyses of eleven selected samples were performed using an ELAN 9000 ICP-MS at the Geoscience Laboratories, Ontario Geological Survey, Sudbury, Canada, following the analytical protocols of Burnham and Schweyer (2004). The composition of the

Table 1 Quality control results of trace and REE analyses showing the composition of measured and certified values of in-house (MRB-29) and international standard (AGV-2), as well as detection limits (DL), Relative Standard Deviations (RSD), and blank values for each element

	Blank	Standards				DL	RSD%
		In-House		International			
		MRB-29 Mesured	MRB-29 Certified	AGV-2 Mesured	AGV-2 Certified		
Sc	0.6	37.8	29	14.9	13	1.1	1.87
Ti	3	11,657	11,511	6,285	6,300	7	1.83
V	1	309.8	312	126.2	120	0.8	1.53
Cr	3	295	255	21	17	3	2.34
Co	0.17	53.72	47	17.14	16	0.13	1.87
Ni	2.6	119.6	91	22.7	19	1.6	1.07
Cu	2.4	141.4	150	50.8	53	1.4	0.83
Zn	2	105	117	84	86	7	1.97
Ga	0.02	19.23		20.42	20	0.04	1.03
Rb	0.04	14.59	13.9	68.38	68.6	0.23	0.77
Sr	0.2	305	312	656	658	0.6	0.80
Y	0.03	27.64	25.1	19.83	20	0.05	0.74
Zr	2	172	174	235	230	6	1.57
Nb	0.006	12.359	13.9	13.361	15	0.028	0.94
Cs	0.001	0.246		1.171	1.16	0.013	1.08
Ba	0.4	288.8	289	1141.7	1,140	0.8	0.99
La	0.05	22.59	20.38	38.89	38	0.04	1.25
Ce	0.1	50.95	48.85	71.35	68	0.12	0.55
Pr	0.012	6.65	6.3	8.406	8.3	0.014	0.37
Nd	0.04	28.27	27.68	31.47	30	0.06	0.96
Sm	0.009	6.436	6.21	5.739	5.7	0.012	1.28
Eu	0.0025	1.9944	1.94	1.657	1.54	0.0031	0.83
Gd	0.007	6.097	5.46	4.638	4.69	0.009	0.57
Tb	0.0001	0.9258	0.83	0.6393	0.64	0.0023	2.14
Dy	0.004	5.448	5.1	3.593	3.6	0.009	1.05
Ho	0.001	1.0434	1	0.6911	0.71	0.0025	1.39
Er	0.003	2.871	2.55	1.876	1.79	0.007	1.50
Tm	0.0004	0.3966	0.37	0.2614	0.26	0.0019	1.53
Yb	0.002	2.478	2.35	1.668	1.6	0.009	0.26
Lu	0.0005	0.3563	0.35	0.248	0.25	0.002	0.50
Hf	0.06	4.35	4.72	5.06	5.08	0.14	1.09
Ta	0	0.744	0.83	0.772	0.89	0.023	1.26
Pb	0	4.7		12.8	13	0.6	2.04
Th	0.002	2.657		6.316	6.1	0.018	1.48
U	0.008	0.675		1.994	1.88	0.011	0.88

reference samples (MRB-29, AGV-2) were analyzed as an unknown during the same analytical runs as the Harmancık samples. Quality control results for MRB-29 in-house reference material and AGV-2 international reference material agree well with the recommended values, and are reported in Table 1 with certified values. Detection limits of each element, average blank values and RSD (%) values are also given in Table 1.

More than 1,000 points were analyzed from spinel and silicate phases by WDS mode using a Superprobe Jeol JXA 8,200 at the "Eugen F. Stumpfl Laboratory" at the Montanuniversitaet Leoben (Austria), operated at 15 kV and 10 nA. The analysis of the samples for Si, Ti, Al, Cr, Fe, Mn, Ni, Mg, Ca, Na, K was carried out using the Kα lines, and were calibrated on natural K-feldspar, albite, diopside, ferrian-chromite, rhodonite, ilmenite and metallic Ni. The counting times for peak and background were 20 and 10 seconds respectively. The amount of Fe^{3+} in the spinel was calculated assuming the ideal spinel stoichiometry, $A^{2+}B^{3+}{}_2O_4$. Detection limits of the oxides are 0.02 wt.% for Si, Al and K, 0.03 wt.% for Ti, Mg, Ca and Na, 0.07 wt.% for Cr and Fe, 0.08 for Mn and 0.11 for Ni.

Results

Petrography

The analyzed peridotite samples are composed mainly of clinopyroxene-poor lherzolites and clinopyroxene-poor harzburgites (Table 2) that are variably serpentinized. The lherzolite samples are poor in clinopyroxene and have the primary modal mineralogy of 60–80 vol.% olivine, 20–30 vol.% orthopyroxene, 5–8 vol.% clinopyroxene, and up to 3 vol.% spinel. Olivine is present as porphyroclastic grains (<3 mm) and smaller neoblasts (<0.4 mm), both of which have kink-band boundaries. Large orthopyroxene grains (up to 5 mm) are generally fresh and show clinopyroxene exsolution lamellae and kink bands. Clinopyroxene porphyroclasts (<3 mm) are typically surrounded by fine-grained olivine and pyroxene neoblasts. Subhedral to unhedral spinel forms disseminated grains (<1 mm), coexisting with clinopyroxene, orthopyroxene, and olivine.

The harzburgitic samples show porphyroclastic textures and consist of olivine (75–85 vol.%), orthopyroxene (15–20 vol.%), clinopyroxene (<3 vol.%), and spinel (1–1.5 vol.%). Olivine

Table 2 Modal abundance and average compositions of minerals, and whole rock (WR) Al_2O_3 and CaO concentrations of the mantle peridotite samples from the Harmancık ophiolite

	Modal Abundances				WR	WR	Ol	Opx	Cpx	Spl
	Ol vol.%	Opx vol.%	Cpx vol.%	Spl vol.%	Al_2O_3 wt.%	CaO wt.%	Fo	Al_2O_3 wt.%	Al_2O_3 wt.%	Cr#
Lherzolite										
H2	63.1	30.6	3.9	2.4	1.95	2.11	90.3	3.83	3.92	21.2
H4	52.7	41.2	3.7	2.4	1.86	0.04				
H5	53.3	40.1	4.3	2.3	2.21	0.04				
H10A	60.0	34.9	3.2	1.9	1.58	1.68	90.7	3.49	3.45	22.5
H11A	58.6	35.4	3.8	2.2	2.13	2.05	90.5	4.02	4.00	18.3
H19	69.3	25.1	3.8	1.8	1.78	1.94	90.3	4.45	4.84	21.2
H20	63.9	30.1	3.9	2.1	1.84	0.73	90.3	4.10	4.26	21.6
H21	62.4	31.3	4.2	2.1	2.17	2.26	90.5	4.44	5.56	19.3
H22	63.4	30.0	4.3	2.3	2.02	2.31	90.0	3.65	3.73	21.2
H23	71.8	22.2	3.9	2.1	1.99	1.99	90.2	4.26	2.90	28.5
Harzburgite										
H1	67.3	29.9	0.9	1.9	0.75	0.58	91.7	2.21		54.7
H3	55.7	42.0	0.0	2.3	0.94	0.05	91.0			36.9
H6	59.0	38.5	0.0	2.5	1.02	0.05				46.1
H7	58.2	39.9	0.0	1.9	0.95	0.04				
H8	57.5	40.5	0.0	2.0	1.35	0.02				
H13	65.3	29.3	3.4	2.0	0.94	1.30				
H14	58.2	40.0	0.0	1.8	1.16	0.02				
H15	70.0	25.8	2.2	2.0	1.07	1.07	91.0	2.95	2.96	40.8
H16	74.2	22.3	1.6	1.9	0.85	0.83	91.3	2.52	2.53	48.9
H17A	74.0	23.3	1.1	1.6	0.89	0.70	90.1	2.57	3.37	53.1
H18	65.6	32.6	0.1	1.7	1.4	0.7				

$Fo = 100 \times Mg/(Mg+Fe^{2+})$;
$Cr\# = 100 \times Cr/(Cr+Al)$;
Ol Olivine; *Opx* Orthopyroxene; *Cpx* Clinopyroxene; *Spl* Spinel. Modal abundances of the mantle phases have been determined by point counting on thin sections at 1 mm point spacing (serpentine minerals were assumed to be after olivine)

grains (up to 6 mm) in these rocks are the most extensively serpentinized minerals and are divided into numerous small grains by a serpentine mesh texture (Fig. 2a). The degree of serpentinization of the harzburgite samples locally attains 74 % in volume. Despite the variable degrees of alteration, we could recognize the primary large crystals of orthopyroxene (Fig. 2b) and olivine relics in all samples. In most of the samples, olivine and orthopyroxene grains display wavy extinction and kink banding. Exsolution of clinopyroxene in orthopyroxene is common in harzburgite samples (Fig. 2c). Primary relict clinopyroxene grains (Fig. 2d) are smaller in size (<2 mm) than orthopyroxene (<5 mm). Subhedral to unhedral, and locally elongated spinels (Fig. 2e and f) are rimmed by thin, ferrian chromite (Fig. 2f), and are the least affected by serpentinization.

Mineral chemistry

Olivine

In the lherzolite samples, the relics of olivine grains range in composition from $Fo_{88.8}$ to $Fo_{91.1}$ (avg. $Fo_{90.3}$; σ=0.38) with NiO and MnO contents of 0.26–0.53 wt.% (avg. NiO=0.38; σ=0.05) and 0.08–0.20 wt.% (avg. MnO=0.14; σ=0.03), respectively. Olivine in the harzburgite samples has slightly higher Fo (89.6–91.8; avg. $Fo_{90.4}$; σ=0.55) and NiO contents (0.34–0.52 wt.%; avg. NiO=0.43 wt.%; σ=0.04), and almost similar MnO contents (0.04–0.19 wt.%; avg. MnO=0.11; σ=0.03) in comparison to the olivine in the lherzolite samples. The Ca content of olivine grains in both the lherzolite and harzburgite samples is very low (<0.07 wt.% CaO) (Table 3).

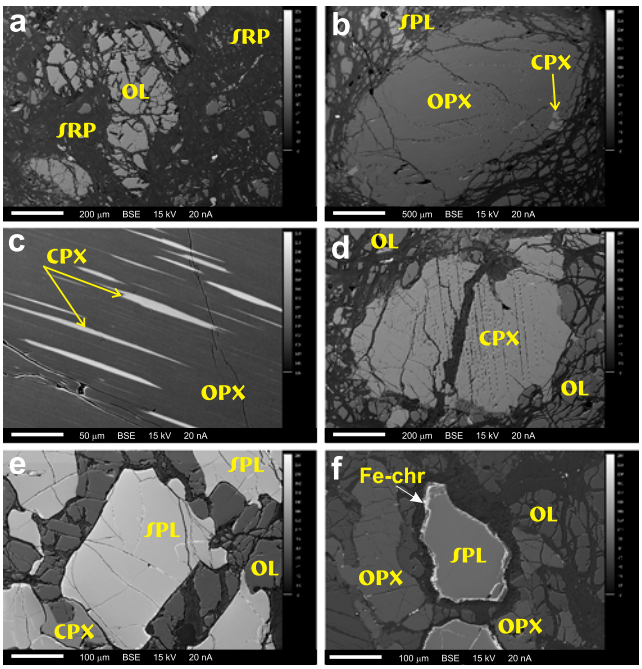

Fig. 2 **a-f** Back scattered electron images from polished thin sections of the peridotite samples. **a** Highly serpentinized olivine grain and serpentine veins, **b** A Large orthopyroxene grain replaced by fine-grained clinopyroxene along its rims in harzburgite (sample H3), **c** Exsolution lamellae of clinopyroxene in orthopyroxene in harzburgite (sample H1), **d** Primary clinopyroxene porphyroblasts in a depleted lherzolite (sample H11A), **e** Subhedral spinel grains coexisting with small clinopyroxene and olivine porphyroblasts in a depleted lherzolite (sample H2), and **f** Spinel grains, with alteration rims of Fe-chromite, coexisting with orthopyroxene and olivine porphyroblasts in a depleted harzburgite (sample H8). Ol: olivine, Opx: orthopyroxene, Cpx: clinopyroxene, Spl: spinel, Fe-chr: Ferrian chromite

Pyroxene

Pyroxenes in the lherzolite and harzburgite consist of enstatitic orthopyroxene ($En_{83.6–90.48}Wo_{0.43–5.30}$) and diopsidic clinopyroxene ($En_{40.7-53.0}Wo_{41.0–51.5}$). Both pyroxenes have almost similar concentrations of Cr in the lherzolite and harzburgite (0.12–1.82 wt.% Cr_2O_3), but pyroxenes in the harzburgite samples have higher Cr# [100×Cr/(Cr+Al); $Cr\#_{opx}$=8.7–20.6; avg. 15.3 and σ=2.41, and $Cr\#_{cpx}$=12.6–27.7; avg. 20.9 and σ=2.63] than those in the lherzolite ($Cr\#_{opx}$=4.0–12.6; avg. 9.5 and σ=1.1, and $Cr\#_{cpx}$=9.3–20.0; avg. 13.1 and σ=1.5) (Tables 4 and 5). The Cr# of pyroxenes displays positive correlations with the Cr# of spinels (not shown). This observation suggests that pyroxene and spinel in these rocks were equilibrated, consistent with a mantle residual origin of the peridotites. The Al_2O_3 content in orthopyroxene varies between 1.64–4.90 wt.% in the lherzolites (avg. 3.89 wt.%; σ=0.59), and is lower in the harzburgites (1.47–4.64 wt.%; avg. 2.62 and σ=0.47). Clinopyroxene also shows a higher Al_2O_3 content in the lherzolites (2.44–6.09 wt.%; avg. 4.09 and σ=0.76) than in the harzburgites (1.88–3.70 wt.%; avg. 2.93 and σ=0.40). The CaO content of orthopyroxene is higher in the lherzolites (0.35–2.65 wt.%; avg. 0.92 and σ=0.37) than those in the harzburgites (0.23–2.00 wt.%; avg. 0.80 and σ=0.38). Similarly, the Na_2O content in clinopyroxene in the lherzolites is higher (0.20–0.64 wt.%; avg. 0.36 and σ=0.09) than those in the harzburgites (0.20–1.22 wt.%; avg. 0.40 and σ=0.20) (Tables 4 and 5). The mantle-derived clinopyroxenes plot in the field corresponding to suboceanic peridotites (Fig. 3) in the Na vs. Cr diagram of Kornprobst et al. (1981).

Spinel

The spinel shows a wider compositional variation than the silicates. The lherzolite samples are represented by spinel with low Cr# (16.4–25.3; avg. 21.1 and σ=1.7) and high Mg# (67.1–79.1; avg. 74.0 and σ=2.7), whereas the harzburgite samples contain spinel with higher Cr# (36.6–58.6; avg. 49.5 and σ=5.7) and lower Mg# (30.9–68.1; avg. 55.0 and σ=.2) (Table 6). The spinels in the lherzolite samples plot in the undepleted end of the abyssal peridotite field of Dick and Bullen (1984) and Arai (1994), whereas the spinel in the

Table 3 Average composition (wt.%) and related cation distribution of olivine from the peridotite samples of the Harmancık ophiolite

	Harzburgite					Lherzolite								DL
Sample	H-1	H3	H15	H16	H17A	H2	H10A	H11	H19	H20	H21	H22	H23	
N	7	11	8	8	15	25	28	38	16	10	26	11	16	
SiO_2	41.18	40.06	40.47	40.98	40.70	39.89	40.25	39.96	40.20	40.65	40.39	40.29	40.65	0.02
Al_2O_3	–	–	0.03	–	–	–	–	–	0.06	–	0.06	–	–	0.02
FeO	8.34	8.93	8.88	8.58	9.16	9.41	9.24	9.54	9.67	9.42	9.23	9.43	9.41	0.07
MnO	0.14	0.11	0.13	0.09	0.09	0.14	0.13	0.15	0.14	0.13	0.20	0.12	0.13	0.08
NiO	0.42	0.39	0.45	0.46	0.44	0.41	0.39	0.37	0.39	0.38	0.39	0.40	0.42	0.11
MgO	51.42	50.88	50.43	50.42	49.18	49.82	50.49	49.93	50.38	50.22	49.51	49.23	48.71	0.03
CaO	–	–	0.03	–	–	–	–	–	0.04	0.05	0.06	0.03	0.05	0.03
Total	101.51	100.37	100.43	100.54	99.56	99.67	100.56	99.95	100.90	100.90	99.83	99.50	99.36	
Si	0.989	0.978	0.986	0.995	0.999	0.983	0.982	0.982	0.979	0.988	0.991	0.992	1.002	
Al	0.000	0.000	0.001	0.000	0.000	0.000	0.000	0.000	0.002	0.000	0.002	0.000	0.000	
Fe^{2+}	0.168	0.182	0.181	0.174	0.188	0.194	0.189	0.196	0.197	0.192	0.189	0.194	0.194	
Mn	0.003	0.002	0.003	0.002	0.002	0.003	0.003	0.003	0.003	0.003	0.004	0.003	0.003	
Ni	0.008	0.008	0.009	0.009	0.009	0.008	0.008	0.007	0.008	0.007	0.008	0.008	0.008	
Mg	1.842	1.851	1.832	1.825	1.802	1.829	1.836	1.829	1.830	1.819	1.812	1.808	1.789	
Ca	0.000	0.000	0.001	0.000	0.000	0.000	0.000	0.000	0.001	0.001	0.002	0.001	0.001	
Total	3.010	3.021	3.013	3.005	3.000	3.017	3.017	3.017	3.019	3.011	3.008	3.006	2.997	
Fo	91.66	91.0	91.0	91.3	90.5	90.4	90.7	90.3	90.3	90.5	90.5	90.3	90.2	

$Fo = 100 \times Mg/(Mg+Fe^{2+})$, *N* number of point analyses from each sample, −: below detection limit, *DL* Detection limits

Table 4 Average composition (wt.%) and related cation distribution of orthopyroxene from the peridotite samples of the Harmancık ophiolite

	Harzburgite							Lherzolite					DL
N	H1 24	H15 25	H16 22	H17A 35	H10A 25	H11A 12	H19 25	H20 25	H21 22	H22 56	H2 12	H23 9	
SiO_2	54.49	54.36	54.59	56.33	54.75	54.76	54.43	54.83	52.98	55.71	55.14	54.83	0.02
TiO_2	0.04	–	0.03	0.04	–	0.04	0.05	0.04	0.05	0.04	0.06	0.06	0.03
Al_2O_3	2.21	2.95	2.52	2.57	3.49	4.02	4.45	4.10	4.44	3.65	3.83	4.26	0.02
Cr_2O_3	0.66	0.67	0.61	0.84	0.51	0.57	0.73	0.67	0.65	0.59	0.58	0.76	0.07
FeO	5.82	6.02	6.11	6.00	6.28	5.88	6.22	6.08	6.03	6.22	5.83	5.93	0.07
MnO	0.14	0.15	0.14	0.09	0.15	0.12	0.14	0.15	0.14	0.12	0.10	0.09	0.08
MgO	33.75	33.99	34.41	32.67	33.91	33.37	32.90	33.78	32.44	33.32	33.48	33.04	0.03
CaO	0.88	0.39	0.69	1.31	0.83	0.80	1.51	0.86	1.02	0.92	0.52	1.10	0.03
Na_2O	–	–	–	0.04	–	0.09	0.03	–	0.03	0.04	0.02	0.03	0.03
Total	98.00	98.52	99.11	99.90	99.91	99.64	100.46	100.50	97.78	100.60	99.56	100.11	
Si	1.922	1.907	1.906	1.947	1.896	1.898	1.880	1.887	1.877	1.913	1.909	1.893	
Ti	0.001	0.000	0.001	0.001	0.000	0.001	0.001	0.001	0.001	0.001	0.002	0.002	
Al	0.092	0.122	0.104	0.105	0.143	0.164	0.181	0.166	0.185	0.148	0.156	0.174	
Cr	0.018	0.019	0.017	0.023	0.014	0.016	0.020	0.018	0.018	0.016	0.016	0.021	
Fe^{2+}	0.172	0.176	0.179	0.173	0.182	0.171	0.180	0.175	0.179	0.179	0.169	0.171	
Mn	0.004	0.005	0.004	0.003	0.004	0.003	0.004	0.004	0.004	0.003	0.003	0.003	
Mg	1.775	1.777	1.793	1.683	1.751	1.724	1.693	1.733	1.714	1.706	1.728	1.701	
Ca	0.033	0.015	0.026	0.049	0.031	0.030	0.056	0.032	0.039	0.034	0.019	0.041	
Na	0.000	0.000	0.000	0.003	0.000	0.006	0.002	0.000	0.002	0.003	0.001	0.002	
Total	4.018	4.019	4.029	3.986	4.021	4.012	4.017	4.016	4.019	4.003	4.003	4.006	
Wo	1.7	0.7	1.3	2.6	1.6	1.6	2.9	1.6	2.0	1.8	1.0	2.1	
En	89.6	90.3	89.8	88.3	89.2	89.6	87.8	89.4	88.7	88.9	90.2	88.9	
Fs	8.7	9.0	9.0	9.1	9.3	8.9	9.3	9.0	9.3	9.3	8.8	9.0	
Mg#	91.2	91.0	90.9	90.7	90.6	91.0	90.4	90.8	90.5	90.5	91.1	90.8	
Cr#	16.7	13.2	14.0	18.0	8.8	8.7	9.9	9.8	8.9	9.8	9.2	10.6	

N number of point analyses from each sample; Mg#= 100×Mg/(Mg+Fe^{2+}), Cr#= 100×Cr/(Cr+Al), En= 100×Mg/(Mg+Fe^{2+}+Ca) Fs= 100×Fe^{2+}/(Mg+Fe^{2+}+Ca), Wo= 100×Ca/(Mg+Fe^{2+}+Ca), −: below detection limit, *DL* Detection limits

harzburgite samples plot within the overlap area between the depleted end of the abyssal peridotite field and the undepleted end of the supra-subduction zone (SSZ) peridotite field of Ishii et al. (1992) and Parkinson and Pearce (1998) (Fig. 4).

The TiO_2 content of spinel is low in the lherzolite samples (<0.10 wt.%; avg. 0.03 and σ=0.02), but spinel in the harzburgite samples may reach up to 0.22 wt.% TiO_2 (avg. 0.12 and σ=0.05) although some harzburgite samples contain spinel with TiO_2 contents as low as those in the lherzolites. The MnO content of spinel is lower in the lherzolites (<0.19 wt.%; avg. 0.10 and σ=0.03) than in the harzburgite samples (<0.30 wt.%; avg. 0.16 and σ=0.04), whereas the NiO content is higher in the lherzolites (0.16–0.38 wt.%; avg. 0.27 and σ =0.04) than in the harzburgite samples (<0.25 wt.%; avg. 0.12 and σ=0.04). The Fe^{3+}# [=100×Fe^{3+}/(Cr+Al+Fe^{3+})] of spinel is low (less than 5.5) in both the lherzolite and harzburgite samples, but the harzburgites contain spinel with slightly higher Fe^{3+}# than the lherzolite samples (Table 6). The TiO_2, MnO and Fe^{3+}# correlate positively with Mg#, whereas NiO displays a negative correlation.

Whole-rock chemistry

Major oxides and trace elements

The whole-rock major, trace, and REE analyses of representative peridotite samples are listed in Table 7. The rock samples are serpentinized to varying extents as indicated by a wide range of loss of ignition (LOI) values between 7.50 and 15.90 wt.%. We present the major oxides on a volatile-free basis to reduce the effect of variable element dilution caused by serpentinization. The whole-rock Mg# values of the lherzolite samples are lower (88.2–90.4; avg. 89.5 and σ =0.64) than those of the harzburgite samples (89.0–91.2; avg. 90.3 and σ=0.70). As expected, the Al_2O_3 and CaO concentrations in the lherzolite samples (1.58–2.21 wt.%, avg. 1.93 and σ=0.2, and 0.73–2.31 wt.%, avg.

Table 5 Average composition (wt.%) and related cation distribution of clinopyroxene from the peridotite samples of the Harmancık ophiolite

	Harzburgite			Lherzolite							DL
N	H15 19	H16 20	H17A 14	H10A 21	H19 20	H20 15	H21 22	H22 56	H2 12	H11A 11	H23 10	
SiO_2	51.82	51.71	53.41	50.20	50.27	50.81	51.49	52.59	52.78	52.05	52.95	0.02
TiO_2	0.04	0.09	0.11	0.07	0.14	0.12	0.11	0.12	0.18	0.12	0.15	0.03
Al_2O_3	2.96	2.53	3.23	3.45	4.84	4.26	5.55	3.74	3.92	4.00	2.90	0.02
Cr_2O_3	1.07	0.92	1.55	0.80	1.04	0.98	1.07	0.86	0.80	0.70	1.11	0.07
FeO	1.97	2.21	2.37	2.71	2.58	2.31	2.86	2.28	2.29	2.35	2.53	0.07
MnO	0.08	0.08	–	0.08	0.09	0.09	0.10	–	–	–	–	0.08
MgO	17.05	17.74	16.33	19.25	16.73	16.92	18.02	16.79	16.99	17.07	18.18	0.03
CaO	23.98	23.49	22.70	21.14	22.48	22.77	20.43	23.07	22.75	22.38	21.82	0.03
Na_2O	0.27	0.29	0.63	0.28	0.39	0.42	0.50	0.32	0.27	0.44	0.26	0.03
Total	99.24	99.06	100.33	97.98	98.55	98.69	100.12	99.77	99.97	99.10	99.90	0.38
Si	1.904	1.904	1.932	1.863	1.859	1.875	1.861	1.912	1.911	1.903	1.920	
Ti	0.001	0.003	0.003	0.002	0.004	0.003	0.003	0.003	0.005	0.003	0.004	
Al	0.128	0.110	0.138	0.151	0.211	0.185	0.237	0.160	0.167	0.172	0.124	
Cr	0.031	0.027	0.044	0.023	0.030	0.028	0.031	0.025	0.023	0.020	0.032	
Fe^{2+}	0.060	0.068	0.072	0.085	0.080	0.071	0.086	0.069	0.069	0.072	0.077	
Mn	0.002	0.002	0.000	0.003	0.003	0.003	0.003	0.000	0.000	0.000	0.000	
Mg	0.934	0.974	0.881	1.072	0.923	0.931	0.968	0.910	0.917	0.931	0.982	
Ca	0.944	0.926	0.880	0.837	0.891	0.900	0.794	0.899	0.883	0.877	0.848	
Na	0.019	0.021	0.044	0.020	0.028	0.030	0.035	0.023	0.019	0.031	0.019	
Total	4.024	4.034	3.993	4.056	4.028	4.028	4.018	4.000	3.995	4.010	4.004	
Wo	48.7	47.1	48.0	42.0	47.1	47.3	43.0	47.9	47.2	46.7	44.5	
En	48.2	49.5	48.1	53.8	48.7	48.9	52.4	48.5	49.1	49.5	51.5	
Fs	3.1	3.5	3.9	4.3	4.2	3.7	4.7	3.7	3.7	3.8	4.0	
Mg#	93.9	93.5	92.5	92.7	92.0	92.9	91.8	92.9	93.0	92.8	92.8	
Cr#	19.6	19.6	24.3	13.4	12.6	13.3	11.5	13.4	12.0	10.5	20.4	

N number of point analyses from each sample; Mg#= 100×Mg/(Mg+Fe^{2+}), Cr#= 100×Cr/(Cr+Al), En= 100×Mg/(Mg+Fe^{2+} +Ca), Fs= 100×Fe^{2+} /(Mg+Fe^{2+} +Ca), Wo= 100×Ca/(Mg+Fe^{2+} +Ca), −: below detection limit, *DL* Detection limits

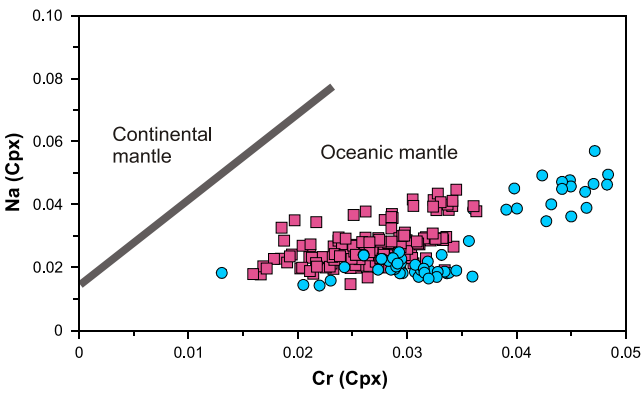

Fig. 3 Na vs. Cr plot for the mantle-derived clinopyroxenes (Kornprobst et al. 1981), showing the composition of clinopyroxenes in the Harmancık upper mantle peridotites. The Harmancık samples plot in the field corresponding to suboceanic peridotites. Symbols used in all figures are as follows: pink square for depleted lherzolite, blue circle for depleted harzburgite

1.90 and σ =0.5, respectively) are higher than in the harzburgites (0.75–1.44 wt.%, avg. 1.00 and σ=0.2, and 0.58–1.30 wt.%, avg. 0.90 and σ=0.3, respectively), although some samples of both rock types have very low CaO contents for a given Al_2O_3 content as a result of Ca depletion during serpentinization (Fig. 5; Table 7). On the basis of CaO and Al_2O_3 concentrations, all lherzolite samples that retained CaO plot within the less depleted abyssal peridotite field, whereas some harzburgite samples plot within the lower end of the abyssal peridotite field (Fig. 5). However, two of the harzburgite samples plot barely within the forearc peridotite field although none of the analyzed harzburgite samples has a highly refractory character.

The whole-rock major, trace, and rare earth element contents of the peridotites are plotted against MgO, and are compared with those of the peridotites recovered from the Izu-Bonin-Mariana forearc system in the Western Pacific

Table 6 Average composition (wt.%) and related cation distribution of spinel from the peridotite samples of the Harmancık ophiolite

	Harzburgite						Lherzolite								DL
N	H1 23	H3 8	H6 16	H15 18	H16 22	H17A 35	H2 7	H10A 25	H11A 8	H19 22	H20 24	H21 18	H22 24	H23 21	
SiO_2	0.09	0.08	0.02	0.39	0.18	0.04	0.04	0.18	0.04	0.08	0.06	0.26	0.05	0.03	0.02
TiO_2	0.16	0.05	0.10	0.03	0.14	0.11	0.07	–	0.08	0.05	0.04	0.04	0.03	0.15	0.03
Al_2O_3	24.81	37.32	28.82	32.31	27.88	25.12	48.41	46.94	51.47	48.38	48.01	49.57	48.65	42.50	0.02
Cr_2O_3	44.67	32.49	36.74	33.19	39.78	42.18	19.44	20.32	17.24	19.35	19.68	17.69	19.46	25.27	0.07
Fe_2O_3	2.36	2.30	3.56	3.02	2.92	1.66	2.58	1.74	1.87	2.18	1.99	1.07	2.55	1.81	
FeO	16.14	13.72	18.07	14.49	15.67	19.58	9.56	11.60	8.96	10.53	11.02	10.04	10.71	11.91	0.07
MnO	0.16	0.18	–	0.14	0.15	–	0.12	0.11	0.18	0.09	0.10	0.09	–	–	0.08
NiO	0.11	0.17	0.12	0.13	0.13	0.10	0.38	0.26	0.43	0.29	0.27	0.31	0.29	0.27	0.11
MgO	13.27	16.16	11.91	14.54	13.69	10.57	19.34	17.87	20.11	18.82	18.40	19.05	18.84	17.29	0.03
Total	101.77	102.46	99.33	98.23	100.54	99.36	99.94	99.01	100.38	99.77	99.56	98.13	100.59	99.22	
Si	0.003	0.002	0.001	0.012	0.005	0.001	0.001	0.005	0.001	0.002	0.002	0.007	0.001	0.001	
Ti	0.004	0.001	0.002	0.001	0.003	0.003	0.001	0.000	0.002	0.001	0.001	0.001	0.001	0.003	
Al	0.876	1.229	1.032	1.131	0.981	0.919	1.533	1.515	1.600	1.537	1.534	1.584	1.537	1.398	
Cr	1.060	0.717	0.882	0.780	0.938	1.038	0.413	0.440	0.359	0.413	0.422	0.379	0.412	0.557	
Fe^{3+}	0.053	0.048	0.081	0.067	0.066	0.039	0.052	0.036	0.037	0.044	0.041	0.022	0.051	0.038	
Fe^{2+}	0.405	0.320	0.459	0.360	0.391	0.510	0.215	0.266	0.198	0.237	0.250	0.228	0.240	0.278	
Mn	0.004	0.004	0.000	0.004	0.004	0.000	0.003	0.003	0.004	0.002	0.002	0.002	0.000	0.00	
Ni	0.003	0.004	0.003	0.003	0.003	0.002	0.008	0.006	0.009	0.006	0.006	0.007	0.006	0.006	
Mg	0.593	0.673	0.539	0.643	0.609	0.489	0.774	0.730	0.790	0.757	0.743	0.770	0.752	0.719	
Total	3.000	3.000	3.000	3.000	3.000	3.000	3.000	3.000	3.000	3.000	3.000	3.000	3.000	3.000	
Mg#	59.4	67.7	54.0	64.1	60.9	49.0	78.3	73.3	80.0	76.1	74.9	77.2	75.8	72.1	
Cr#	54.7	36.9	46.1	40.8	48.9	53.1	21.2	22.5	18.3	21.2	21.6	19.3	21.2	28.5	
Fe^{3+}#	2.7	2.4	4.1	3.4	3.3	1.9	2.6	1.8	1.9	2.2	2.0	1.1	2.6	2.6	

Cr#=100×Cr/(Cr+Al); Mg#=100×Mg/(Mg+Fe^{2+}), Fe^{3+} #=100×Fe^{3+}/(Cr+Al+Fe^{3+}), *N* number of point analyses from each sample, −: below detection limit, *DL* Detection limits

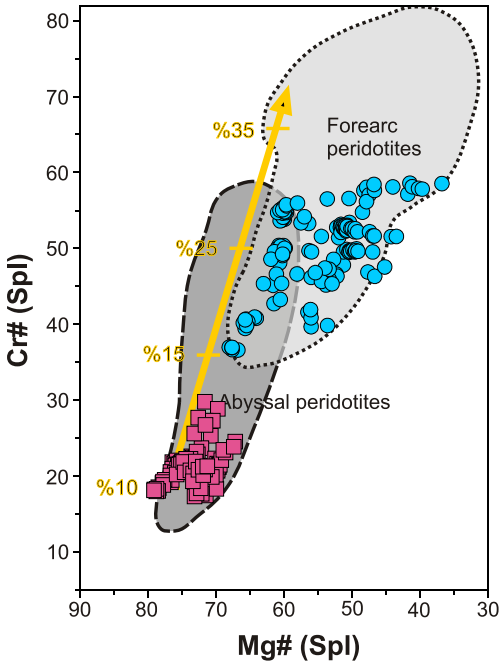

Fig. 4 Spinel compositions of the Harmancık peridotite samples plotted on a Mg# [100×Mg/(Mg+Fe^{2+})] vs. Cr# [100×Cr/(Cr+Al)] diagram. Spinel fields of abyssal (Dick and Bullen 1984; Arai 1994) and forearc peridotites (Ishii et al. 1992; Parkinson and Pearce 1998) are shown for comparison. Partial melting trend (*yellow arrow*) is from Arai (1992)

(Fig. 6). The CaO and Al_2O_3 abundances display well-defined inverse linear correlations with the MgO contents, although the CaO content of some highly serpentinized samples are very low and scatter away from the trend. Elements Y, V and Yb, which are all incompatible during partial melting, also show negative correlations with MgO. Instead, La shows no significant correlation with MgO.

Rare Earth Element (REE) patterns

Primitive Mantle (PM)-normalized REE data of the lherzolite and harzburgite samples are shown in Fig. 7. All samples are characterized by low REE contents with the normalized abundances being less than 1 (REE_N <1) (Fig. 7).

The lherzolite samples display slightly positive slopes from Eu to Lu, and follow partial melting lines. However, the slopes are negative between La and Eu in four out of five lherzolite samples, a fact that is inconsistent with LREE/MREE fractionation in the residua by partial melting (Fig. 7). A lherzolite sample (H21) shows increasing depletion of PM-normalized values towards the more incompatible REE (LREE). Harzburgite samples have lower HREE and MREE concentrations compared to the lherzolite samples, but similarly to the lherzolite samples, they show positive slopes from MREE to HREE (Fig. 7). The patterns of the harzburgite samples resemble those of highly depleted abyssal peridotites or undepleted forearc peridotites from the Izu-Bonin-Mariana (IBM) forearc system with low REE contents that are also enriched in LREEs. The patterns of the lherzolite samples, on the other hand, plot within the field of abyssal peridotites (Pearce et al. 2000), which are characterized by higher HREE concentrations (Fig. 7).

Discussion

Geochemical features of abyssal vs SSZ peridotites

Mineral compositions and geochemistry of the upper mantle peridotites in ophiolites are a key to understand the extent of melt extraction, fluid phase enrichment, and mantle-melt interaction processes subsequent to melt extraction (e.g. Dick 1989; Johnson et al. 1990; Hellebrand et al. 2002; Seyler et al. 2007; Uysal et al. 2007, 2012; Choi et al. 2008; Dilek and Morishita 2009; Morishita et al. 2011b). Abyssal peridotites generally comprise lherzolites and clinopyroxene-rich harzburgites, formed by MORB-type melt extraction as a result of 5-15 % partial melting of fertile mantle under dry conditions (e.g., Dick and Bullen 1984; Johnson and Dick 1992). The melt that is formed due to low- to moderate-degrees of partial melting of a fertile mantle is commonly rich in TiO_2, leaving behind a depleted mantle with Ti-poor and Cr-rich (high Cr#) spinel. The TiO_2 content of residual spinel is expected to decrease with an increase in the Cr# of spinel, as the degree of partial melting increases (e.g. Pearce et al. 2000).

Abyssal peridotites contain spinel with Cr# generally ranging between 10 and 40, and rarely reaching 60. Peridotites from back arc basins have also been reported to have similar spinel compositions to those in normal abyssal peridotites (Ohara et al. 2002; Choi et al. 2008). However, the reaction of subsequently-formed MORB-type melts with the upper mantle peridotites in back arc settings may increase the TiO_2 content of spinel without increasing the Cr# (e.g. Choi et al. 2008). The SSZ peridotites, which are the remnants of much higher degrees of partial melting of the upper mantle above a subducting slab, contain spinel with higher Cr# ranging from 38 to 80 (in rare cases exceeding 90), although there is an overlap from Cr# 38 to 58 between depleted abyssal peridotites and undepleted SSZ peridotites (e.g., Arai 1994; Gaetani and Grove 1998). Due to the higher degrees of partial melting, pyroxenes in SSZ-type peridotites are also expected to be depleted in the moderately incompatible elements Al, Ti, and Na. Olivine in these peridotites also has higher Fo contents. Consistent with mineral chemistry characteristics, the whole rock compositions of these peridotites are more depleted in incompatible elements compared to the abyssal peridotites (e.g., Parkinson et al. 1992; Parkinson and Pearce 1998; Pearce et al. 2000; Uysal et al. 2007, 2012).

Table 7 Whole rock major oxides (wt.%), trace elements and REE concentrations (ppm) in mantle peridotites from the Harmancık (NE Turkey) ophiolite

	Harzburgite														Lherzolite										
	H1	H1-2	H3	H6	H7	H8	H8_Dup	H13	H14	H15	H15_Dup	H16	H17A	H18	H2	H4	H5	H12	H10A	H11A	H19	H20	H21	H22	H23
SiO_2	44.01	43.84	44.72	43.92	44.79	44.23		43.9	44.81	43.22		42.43	42.57	43.89	43.81	44.72	44.18	42.94	43.23	44.5	42.99	43.68	44	44.17	42.83
Al_2O_3	0.75	0.76	0.94	1.02	0.95	1.35		0.94	1.16	1.07		0.85	0.89	1.44	1.95	1.86	2.21	1.61	1.58	2.13	1.78	1.84	2.17	2.02	1.99
Fe_2O_3	7.98	8.06	9.24	9.85	8.49	9.34		8.35	8.26	8.18		8.68	8.67	8.28	9.13	9.59	10.16	10.03	8.88	8.85	8.98	8.96	8.69	8.09	8.44
MnO	0.11	0.1	0.13	0.06	0.13	0.11		0.12	0.13	0.11		0.11	0.09	0.1	0.12	0.1	0.1	0.09	0.12	0.12	0.12	0.1	0.12	0.11	0.12
MgO	46.14	46.22	44.39	44.55	45.13	44.41		44.89	45.17	45.77		46.51	46.54	45.03	42.12	43.15	42.74	44.7	44.08	41.82	43.75	44.21	42.26	42.66	44.03
CaO	0.58	0.59	0.05	0.05	0.04	0.02		1.3	0.02	1.07		0.83	0.7	0.69	2.11	0.04	0.04	0.01	1.68	2.05	1.94	0.73	2.26	2.31	1.99
Na_2O	0.02	0.03	0.01	0.01	0.01	0.01		0.01	0.01	0.01		0.01	0.02	0.01	0.08	0.01	0.01	0.01	0.03	0.03	0.02	0.01	0.05	0.03	0.05
K_2O	0.04	0.04	0.05	0.05	0.05	0.05		,0.04	0.05	0.04		0.04	0.04	0.05	0.04	0.05	0.05	0.05	0.04	0.04	0.04	0.05	0.04	0.04	0.05
P_2O_5	0.01	0.01	0.01	0.01	0.01	0.01		0.01	0.01	0.01		0.01	0.01	0.01	0.01	0.01	0.01	0.01	0.01	0.02	0.01	0.01	0.01	0.01	0.01
Cr_2O_3	0.38	0.37	0.45	0.51	0.41	0.46		0.45	0.39	0.4		0.4	0.36	0.37	0.48	0.47	0.47	0.56	1,325	0.44	0.37	0.41	0.4	0.42	0.39
Total	100.04	100.03	100.02	100.04	100.02	100.01		99.97	100.03	99.9		99.9	99.9	99.89	99.89	100.01	100.01	100.03	100.05	100.02	100.02	100.03	100.03	99.9	99.93
LOI	9.9	9.9	14.6	14.1	15.1	14.6		7.5	14.5	9.4		10.6	10.6	13.4	8.4	15.7	15.9	14.7	9.1	9.8	8.3	12.6	7.6	10.2	13
Srp%	55	55	81	78	84	81		42	81	52		59	59	74	47	87	88	82	51	54	46	70	42	57	72
Mg#	91.2	91.1	89.5	89.0	90.5	89.5		90.5	90.7	90.9		90.5	90.5	90.6	89.2	88.9	88.2	88.8	89.8	89.4	89.7	89.8	89.7	90.4	90.3
Sc	8.7		12			15.6	15.1		10.7	10.8	10.6	6.9			12.9				13.3	14.9		15.6	16.9		
Ti	84		96			51	51		43	76	75	92			143				125	163		119	290		
V	46.7		55.5			66	66		51.3	54.3	55.8	50			73.8				65.1	68.9		72.7	83.2		
Cr	2,548		2,736			3,803	3,782		2,593	3,546	3,696	2,767			2,965				2,954	2,826		3,306	3,140		
Co	119		116			134	134		113	134	133	115			102				115	107		129	133		
Ni	2,328		2,382			3,039	3,043		2,401	2,792	2,729	2,286			1,969				2,335	2,055		2,638	2,589		
Cu	6.2		16.1			11.6	12.4		5	15.5	13.6	6.2			20.8				19.5	8.5		17.8	27.2		
Zn	47		54			46	50		44	42	42	48			40				43	40		63	67		
Ga	0.91		1.36			1.22	1.24		0.90	1.12	1.22	0.81			1.52				1.29	1.54		1.28	1.43		
Rb	<0.23		<0.23			<0.23	<0.24		<0.23	<0.23	<0.24	<0.23			0.25				<0.23	0.44		<0.23	<0.23		
Sr	0.8		1.7			0.8	1.0		2.0	2.0	1.9	0.6			0.9				2.0	3.7		1.5	1.8		
Y	0.14		0.39			0.32	0.34		0.28	0.33	0.32	0.21			0.97				0.84	1.06		0.90	1.67		
Zr	<6		<6			<6	<7		<6	<6	<7	<6			<6				<6	<6		<6	<6		
Nb	<0.028		<0.028			<0.028	<0.029		<0.028	<0.028	<0.029	<0.028			0.032				<0.028	0.042		<0.028	<0.028		
Cs	0.015		<0.013			0.014	0.015		0.014	0.024	0.023	0.015			0.034				0.026	0.08		<0.013	0.017		
Ba	1.6		1.9			1.0	1.3		20.1	3.8	3.8	3.9			1.7				4.1	3.9		2.1	5.2		
La	0.0500		0.0600			0.0400	0.0600		0.1200	0.0700	0.0700	0.0600			0.1400				0.0800	0.2100		0.0700	0.0600		
Ce	0.1300		<0.12			<0.12	0.13		0.1900	0.1400	0.1500	0.1500			0.2900				0.1900	0.4300		0.1400	<0.12		
Pr	0.0140		<0.014			<0.014	0.014		0.0230	0.0180	0.0160	0.0160			0.0370				0.0210	0.0580		0.0190	0.0150		
Nd	0.0700		<0.06			<0.06	0.07		0.0900	0.0700	0.0700	0.0600			0.1300				0.1000	0.2100		0.0800	0.0900		
Sm	0.0190		0.0180			0.0130	0.0170		0.0270	0.0240	0.0220	0.0210			0.0460				0.0340	0.0610		0.0360	0.0810		
Eu	0.0059		0.0075			0.0037	0.0045		0.0094	0.0076	0.0057	0.0064			0.0149				0.0129	0.0204		0.0115	0.0332		
Gd	0.0120		0.0230			0.0200	0.0160		0.0210	0.0330	0.0290	0.0210			0.0780				0.0580	0.1040		0.0570	0.1480		
Tb	0.0028		0.0053			0.0025	0.0044		0.0045	0.0061	0.0066	0.0049			0.0178				0.0140	0.0206		0.0140	0.0338		
Dy	0.0150		0.0490			0.0340	0.0390		0.0320	0.0460	0.0440	0.0320			0.1470				0.0990	0.1630		0.1140	0.2530		
Ho	0.0038		0.0130			0.0110	0.0117		0.0083	0.0118	0.0116	0.0080			0.0382				0.0271	0.0408		0.0304	0.0604		
Er	0.0090		0.0460			0.0410	0.0450		0.0330	0.0440	0.0360	0.0230			0.1230				0.0930	0.1330		0.1030	0.1900		

Table 7 (continued)

	Harzburgite											Lherzolite									
	H1	H1-2	H3	H6	H7	H8	H8_Dup	H13	H14	H15	H15_Dup	H16	H17A	H18	H2	H4	H5	H12	H10A	H11A	H19	H20	H21	H22	H23
Tm	0.0022		0.0084			0.0081	0.0088		0.0058	0.0077	0.0071	0.0038			0.0224				0.0158	0.0229		0.0167	0.0321		
Yb	0.0220		0.0750			0.0670	0.064		0.0500	0.0510	0.0580	0.0280			0.1420				0.1040	0.1530		0.1300	0.2260		
Lu	0.0035		0.0129			0.0123	0.0126		0.0094	0.0103	0.0097	0.0051			0.0266				0.0191	0.0249		0.0212	0.0362		
Hf	<0.14		<0.14			<0.14	<0.15		<0.14	<0.14	<0.14	<0.14			<0.14				<0.14	<0.14		<0.14	<0.14		
Ta	<0.023		<0.023			<0.023	<0.023		<0.023	<0.023	<0.023	<0.023			<0.023				<0.023	<0.023		<0.023	<0.023		
Pb	<0.6		<0.6			<0.6	<0.6		<0.6	<0.6	<0.6	<0.6			<0.6				<0.6	<0.6		<0.6	<0.6		
Th	<0.018		<0.018			<0.018	<0.019		<0.018	<0.018	0.008	<0.018			0.026				<0.018	0.028		<0.018	<0.018		
U	<0.011		<0.011			<0.011	0.011		0.013	0.012	0.013	<0.011			0.018				0.016	0.035		<0.011	0.079		

LOI Loss on ignition, *Mg#*=(mol) 100×MgO/(MgO+FeO), *Serp%*=(100/18)×LOI (wt.%)

Comparison of the Harmancık peridotites with abyssal and SSZ peridotites

On the basis of mineral compositions and whole rock geochemistry, we have recognized two groups of peridotites, i.e. depleted lherzolites and harzburgites, in the exposed upper mantle section in the Harmancık area in NW Turkey. Considering the Fo contents of the olivine and the Cr# values of the spinel, all the analyzed samples fall into the olivine-spinel mantle array (OSMA) described by Arai (1994), indicating that the Harmancık peridotites represent residual material left behind after partial melting of the upper mantle (Fig. 8a). The depleted lherzolites are represented by low Cr# of spinel and a relatively higher content of Al_2O_3 and TiO_2 in pyroxenes. These lherzolites have higher contents of whole-rock CaO and Al_2O_3, consistent with the modal abundance of clinopyroxene. However, the depleted harzburgite samples are characterized by relatively higher Cr# spinel (Fig. 8a). These rocks display a relatively higher Cr_2O_3 content but similar Mg# in clinopyroxene (Fig. 8b), and the Al_2O_3 contents of their orthopyroxene and clinopyroxene are relatively lower than those of the depleted lherzolite samples (Fig. 9a and b). Based on the mineral and whole-rock compositional data, our depleted lherzolite samples clearly plot in the field of fertile abyssal peridotites, whereas the depleted harzburgite samples straddle the boundary between the abyssal and fore-arc peridotite fields (Figs. 6, 7, 8 and 9). Hence, we infer that the Harmancık peridotites show the characteristics of both abyssal and SSZ type peridotites.

Partial melting and melt-peridotite interaction

The degree of partial melting of the studied peridotite samples can be calculated by using their residual mineral and whole-rock compositions. The composition of primary spinels in upper mantle peridotites is generally highly informative. In fact, Cr# reflects the relative degree of the partial melting (e.g., Hellebrand et al. 2001). The low- to moderately-depleted compositions of the lherzolite and harzburgite samples imply that these rocks underwent low (~10–13 %) to moderate (~15–30 %) degrees of partial melting, respectively (Fig. 4). The progressive depletion of rocks in both the Al_2O_3 and HREE contents from the lherzolites to harzburgites provides strong evidence for increasing degrees of melt extraction from the system during partial melting (Figs. 6 and 7). Thus, significant geochemical variations in our lherzolitic and harzburgitic peridotites are largely the result of various degrees of partial melting.

The Harmancık lherzolites have slightly rising MREE-HREE patterns analogous to fertile abyssal peridotites, which is consistent with small amounts of partial melting as shown in Fig. 7. The steeper slopes of MREE-HREE patterns in depleted harzburgite samples indicate relatively higher degrees of partial melting (Fig. 7). Both peridotite types display

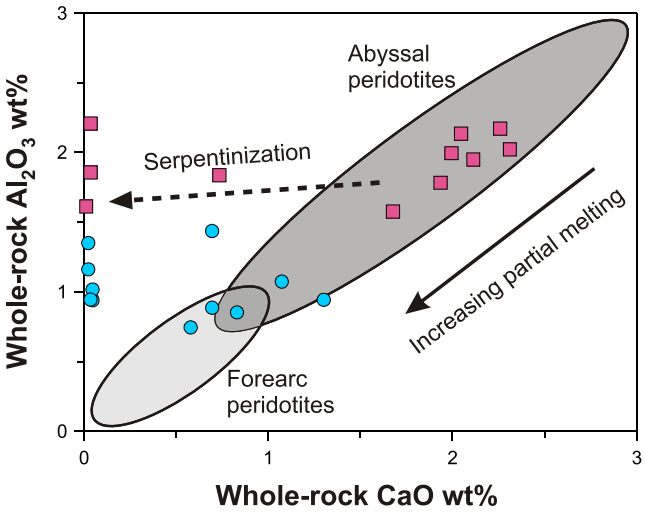

Fig. 5 Whole-rock Al_2O_3 (wt.%) versus CaO (wt.%) plot for the Harmancık peridotites. Abyssal and forearc peridotite fields, as well as the partial melting trend, are taken from Pearce et al. (1992)

LREE enrichments compared to the MREE. This feature is inconsistent with a simple partial melting process, but rather reflects subsequent melt/fluid interaction with mantle rock.

If the peridotites were the products of simple melt extraction, incompatible elements such as TiO_2 should decrease in spinel with an increase in its Cr#, which is a good measure of the degree of partial melting in upper mantle peridotites (Dick and Bullen 1984; Arai 1994). When these peridotites subsequently become affected by reaction with island arc tholeiite (IAT) melts, the TiO_2 contents in spinel show enrichment with increasing Cr# (e.g. Choi et al. 2008). The spinel Cr# versus TiO_2 relationships show that the most refractory harzburgites of the Harmancık peridotites reacted more extensively with percolating melts during porous flow, and that these melts had compositions of subduction-initiation magmas similar to those of the IBM melt compositions in the very early stages of subduction (Fig. 10).

In order to reveal the petrologic processes in the genesis of the Harmancık peridotites, we performed a modelling of non-modal dynamic melting (with open- and closed-system) using the whole-rock trace element data (Fig. 11). Mineral partition coefficients for the models were compiled from McKenzie and O'Nions (1991), Suhr (1999), Green et al. (2000) and Adam and Green (2006). Whole-rock and mineral chemistry of the lherzolitic samples indicate that they

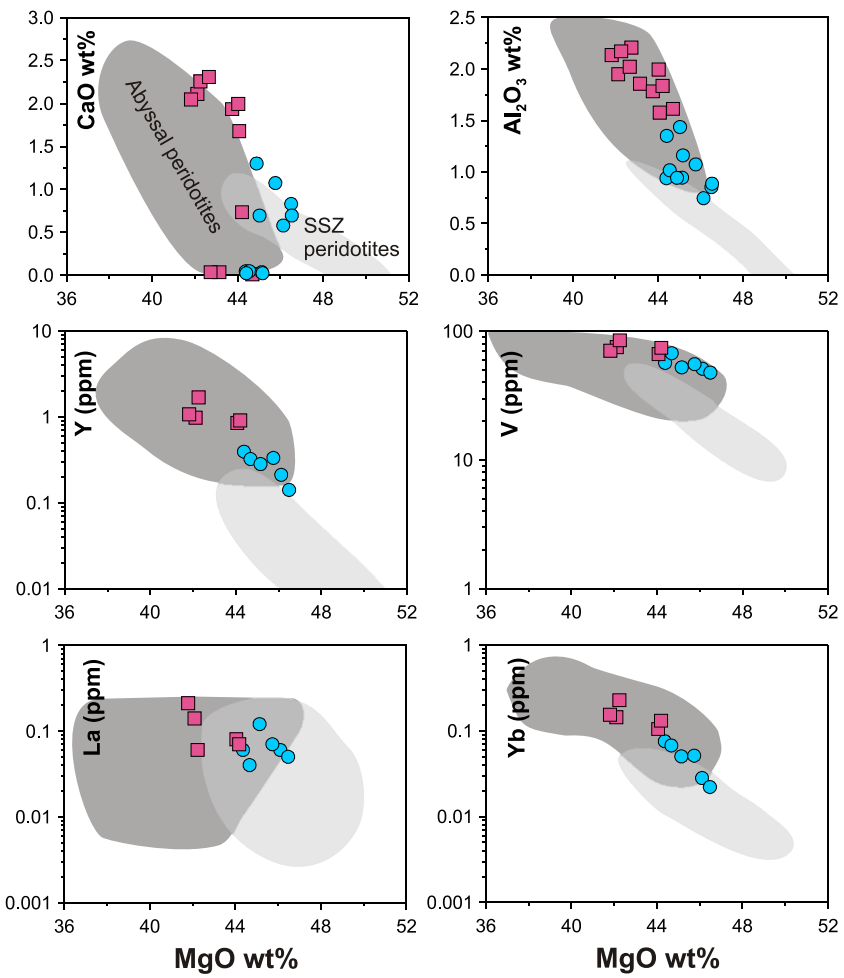

Fig. 6 Variation diagrams of major oxides and trace elements vs. MgO (wt.%) in bulk rock Harmancık peridotite samples. Abyssal (*dark grey*; Niu et al. 1997) and supra-subduction zone peridotite (light grey; Parkinson and Pearce 1998) fields are also shown for comparison

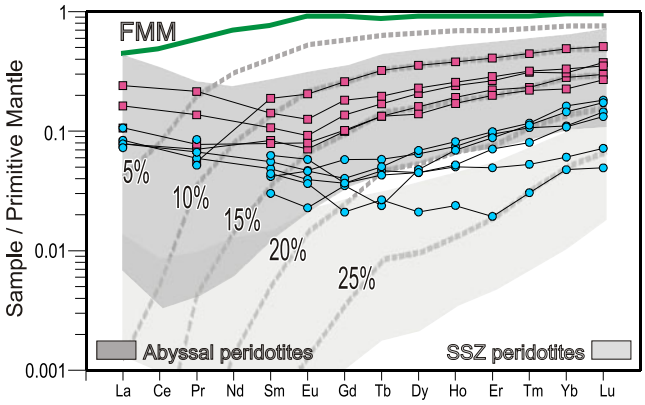

Fig. 7 Primitive Mantle-normalized REE abundances of the Harmancık peridotite samples. Fertile MOR Mantle (FMM; Bedard 1999) composition and partial melting residuals from FMM are also shown. Melting models use non-modal dynamic melting equation with critical melt porosity (Φ) of 1 %, and assume that the source has a spinel facies lherzolitic composition (mineral and melt modes of the spinel lherzolite: $Ol_{0.53(-0.06)}+Opx_{0.27(0.28)}+Cpx_{0.17(0.67)}+Sp_{0.03(0.11)}$; Kinzler 1997). Partition coefficients are compiled from McKenzie and O'Nions (1991), Suhr (1999); Green et al. (2000), Adam and Green (2006). Abyssal (*dark grey*; Niu et al. 1997) and supra-subduction zone peridotite (*light grey*; Parkinson and Pearce 1998) fields are also shown for comparison. Primitive mantle values are from Palme and O'Neil (2004)

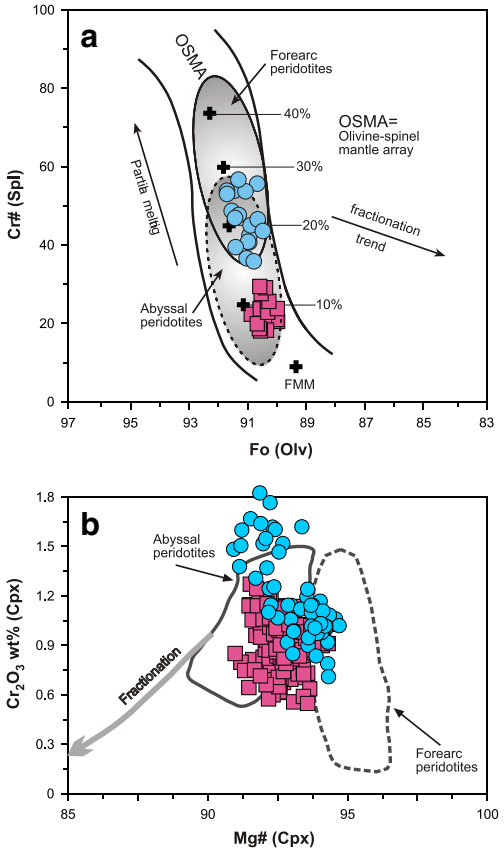

Fig. 8 **a** Plots of Cr# of spinel vs. Fo content of coexisting olivine. Olivine-spinel mantle array and melting trend are from Arai (1994). Abyssal peridotite field from (Dick and Bullen 1984), forearc peridotite field from (Ishii et al. 1992; Parkinson and Pearce 1998; Pearce et al. 2000). **b** Compositional variations of clinopyroxene in two types of peridotites on a Cr_2O_3 vs. Mg# diagram. Abyssal peridotite field from Johnson et al. (1990); forearc peridotite field from Ishii et al. (1992)

most probably represent depleted abyssal-type peridotites formed in a mid-ocean ridge system. Their Ni/Yb ratios with respect to Yb contents are modeled on Fig. 11a. These elements (and their ratios) are not significantly affected by melt/fluid interaction, and are hence highly informative when assessing the degrees of partial melting and depletion events. In the model, the starting composition is Fertile Mid Ocean Ridge Mantle (FMM; Bedard 1999) with spinel lherzolite mineralogy. The mineral and melt modes are O10.53(-0.06)+Opx0.27(0.28)+Cpx0.17(0.67)+Sp0.03(0.11) (Kinzler 1997). Although, the mineral chemistry data indicate that the lherzolites underwent ~10–13 % melting, trace element data indicate ~10–17 % of melting (Fig. 11a).

Unlike the compatible and fluid-immobile element Ni, the highly incompatible and fluid-mobile element La is sensitive to melt/fluid and wall-rock interaction, and instead of Ni/Yb, the ratio of La/Yb is more useful for monitoring the degree of melt/fluid interaction on the mantle residues. Therefore, open-system non-modal dynamic melting model, during which a certain amount of melt or fluid continuously interacts with the residua (Ozawa and Shimuzi 1995; Zou 1998), is applied in Fig. 11b. In this model, mass flux rate (β) is defined as the influxing mass fraction (relative to the initial solid) divided by the degree of melting. Considering the heterogeneous interaction between the fluid/melt and the wall rocks, different values of β can be used. Fluxing material is considered as low-degree (1.5 %) basaltic partial melt derived from FMM itself (calculated by non-modal dynamic melting with critical melt porosity, Φ, of 1 %). We then use this basaltic component as a fluxing component in the open-system dynamic melting models for the lherzolitic samples. In Fig. 11b, the residual compositions obtained from a closed-system dynamic melting model are also shown for comparison with open-system melting. Open-system melting in Fig. 11b is modeled by considering that basaltic melt is fluxed with a β value of 1 %. On the other hand, such fluxing cannot explain the high La/Yb ratios of the Harmancık lherzolitic rocks, as too high β ratios (up to 25 %) are needed. Even such a high fluxing ratio fails in explaining the REE patterns of the lherzolites (see below). This may indicate that the upper mantle peridotites may have interacted with fluid/melts without melting; such processes can be explained by simple mixing processes to have occurred in a subduction system. This discrepancy shall be discussed below. Nevertheless, assuming that the lherzolitic samples were affected by melt/fluid interaction in a subduction system (without melting), the certain model results obtained from the open-system melting (OSM) trend in Fig. 11b are mixed with a subduction zone component (SZC; Eiler et al. 2000, 2007). The results of

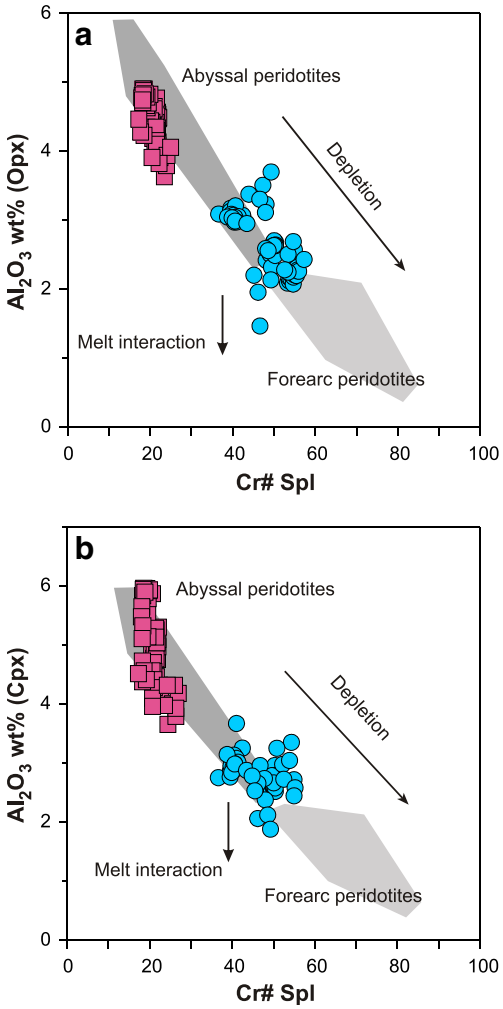

Fig. 9 Plot of Al_2O_3 (wt.%) of orthopyroxene **a**, and clinopyroxene **b** vs. Cr# [100×Cr/(Cr+Al)] of coexisting spinel in the Harmancık peridotites. Abyssal and forearc peridotite fields from Bonatti and Michael (1989) and Parkinson et al. (2003)

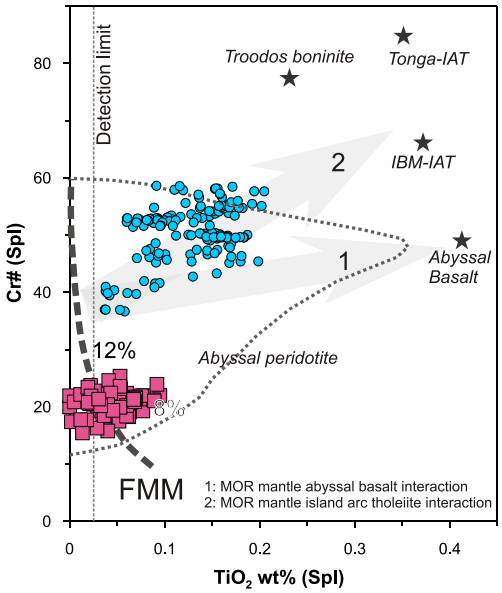

Fig. 10 Cr# [100×Cr/(Cr+Al)] vs. TiO_2 (wt.%) in spinel of the Harmancık peridotites. Grey arrows illustrate the effects of MORB melt (*arrow* 1) and IAT (*arrow* 2) reaction. Data for Tonga-IAT (island arc tholeiite) and IBM (Izu Bonin-Mariana)-IAT from (Pearce et al. 2000). Abyssal peridotite field from (Dick and Bullen 1984). Filled stars represent the spinel compositions in equilibrium with boninite-, IAT- and MORB-type melts

0.05 %, 0.20 % and 0.07 % mixing of SZC with depleted model peridotite compositions with ratios of 10 %, 13 % and 16 %, respectively, are shown (green asterisk; Model-1, Model-2 and Model-3, respectively) in Fig. 11b. These models explain the La/Yb versus Yb systematics of the lherzolitic samples effectively.

The calculated melting models are also illustrated on PM-normalized REE diagrams in Fig. 11c. Among the lherzolitic samples of the Harmancık peridotites. Sample H21 is characterized by the highest HREE contents (indicating the lowest degrees of melting) and the lowest LREE contents (indicating the lowest degrees of refertilization). Except for sample H21, samples H2 and H10A are characterized by the highest and lowest HREE contents, respectively. Taking into account the REE patterns of these 3 samples, the models 1, 2 and 3 are constructed in Fig. 11b. The results suggest that these samples can be considered as the relicts of partial melting in a mid-ocean setting, but they were also affected from melt/fluid and residua interaction in a subduction system without significant degrees of second-stage partial melting in the mantle wedge. Variations in mixing rates and melting degrees might have also resulted from heterogeneities in the melting and enrichment processes.

The harzburgite samples have lower HREE contents compared to the lherzolites which are assumed to be relicts of a first stage, low-degree partial melting residue formed in a MOR setting. On the basis of the whole-rock and mineral chemistry data, we think that a second-stage partial melting and depletion event may have occurred in a supra-subduction zone (SSZ) setting. Therefore, we infer that the Harmancık harzburgites are the partial melting residues of the lherzolites (i.e., the harzburgites most probably represent the second-stage melting residue of the Harmancık lherzolites).

As a first approximation, Ni/Yb ratios and Yb contents of the harzburgites were modeled in Fig. 11d. The starting composition is assumed to be represented by the most depleted lherzolite sample from the Harmancık (sample H10A), and this corresponds to an ~16 % depleted mantle composition in a MOR setting. The mineral and melt modes are Ol0.64(-0.06)+Opx0.27(0.28)+Cpx0.08(0.67)+Sp0.01(0.11), which are calculated for 16 % melting. Approximately 4–11 % closed-system dynamic melting of the depleted mantle (represented by sample H10A) can explain the Ni/Yb vs Yb systematics of the harzburgite samples. An open-system dynamic melting model for the harzburgite sample is also shown on the La/Yb vs Yb diagram (Fig. 11e). The results of the open-system

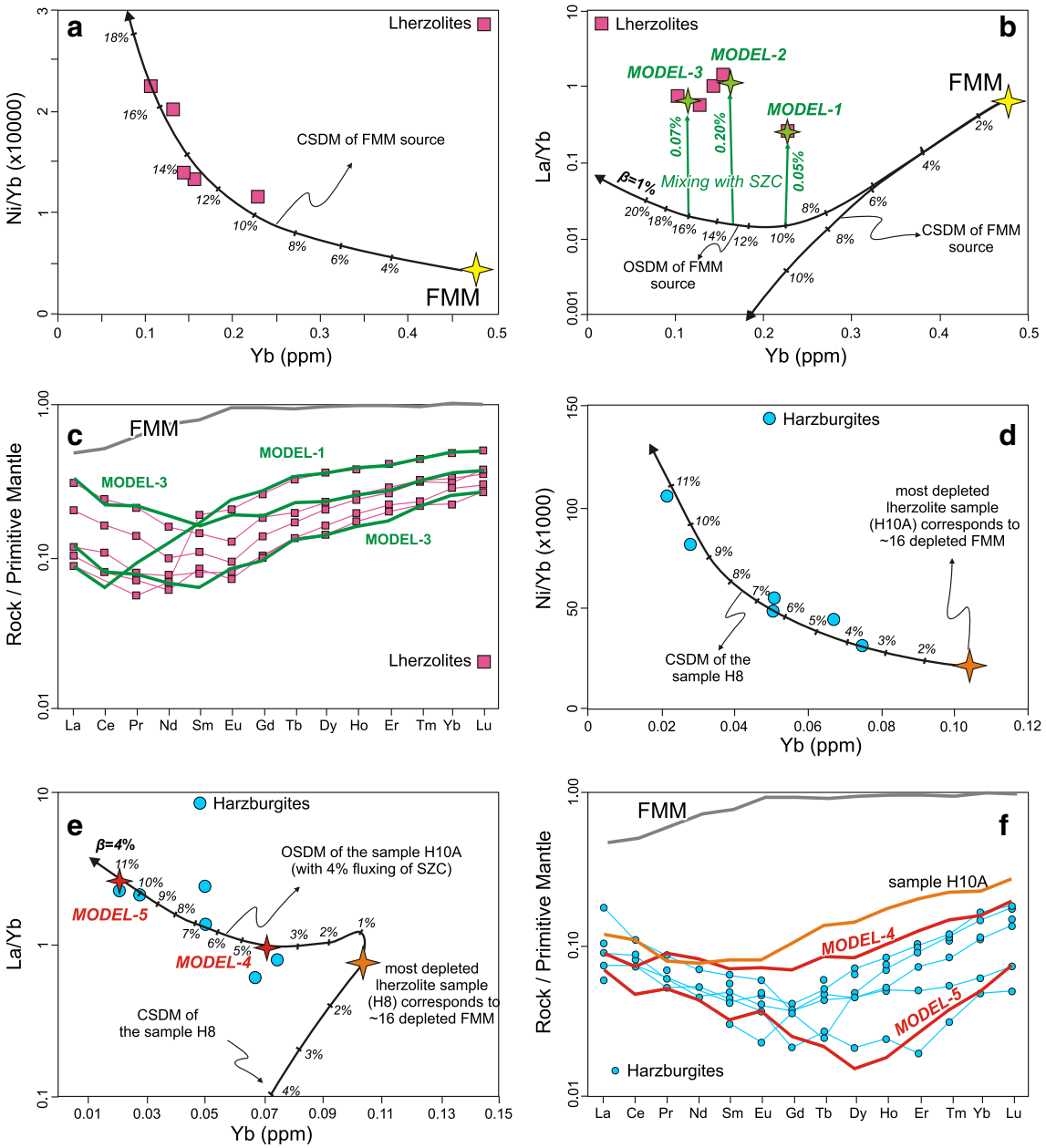

Fig. 11 Closed- and open-system partial melting (CSDM and OSDM, respectively) models for the Harmancık peridotites. Starting composition is Fertile Mid Ocean Ridge Mantle (FMM; Bedard 1999) in (a) to (c) and sample H10A in (d) to (e). Melting models use non-modal dynamic melting equation with critical melt porosity (Φ) of 1 %, and assume that the source has a spinel facies lherzolitic composition (mineral and melt modes: $Ol_{0.53(-0.06)}+Opx_{0.27(0.28)}+Cpx_{0.17(0.67)}+Sp_{0.03(0.11)}$; Kinzler 1997) in (a) to (c) and 16 % depleted spinel facies mantle (mineral and melt modes: $Ol_{0.64(-0.06)}+Opx_{0.27(0.28)}+Cpx_{0.08(0.67)}+Sp_{0.01(0.11)}$). Fluxing material in OSDM models is assumed as low-degree (1.5 %) basaltic partial melt derived from FMM itself in (b) and subduction zone component (SZC; Eiler et al. 2000; 2007) in (e) and (f). Models 1 to 3 in (b and c) are produced by low-degrees (0.05 % to 0.20 %) of simple mixing between SZC and the 10 %, 13 % and 16 % OSDM residuals of FMM, respectively. Models 4 and 5 are produced by 4 % and 11 % OSDM of sample H10A, which is assumed as the starting composition of the second-stage melting. Partition coefficients are compiled from McKenzie and O'Nions (1991), Suhr (1999); Green et al. (2000), Adam and Green (2006). Normalizing values in primitive mantle-normalized diagrams are from Palme and O'Neil (2004)

dynamic melting model show that the harzburgite samples can be produced by ~4–11 % melting of the already 16 % depleted FMM (represented by sample H10A), with β=4 %. The results of the 4 % and 11 % melting models, Model 4 and Model 5, respectively, are also shown on PM-normalized REE diagrams in Fig. 11e. Despite the small discrepancies in individual trace element abundances, the patterns of the models fit well with the data. Here, the high β values (~4 %) for Models 4 and 5,

with respect to mixing ratios in Models 1–3 can be considered as accompanying melting events in a subduction environment.

Tectonic setting of the Harmancık ophiolite

Parkinson et al. (1992), Parkinson and Pearce (1998), and Pearce et al. (2000) have shown that both SSZ and abyssal peridotites may occur in forearc tectonic settings although the former are typically dominant. Peridotites in forearc settings may have a variety of origins, ranging from supra-subduction zone peridotites that equilibrated with hydrous fluids and melts derived from the subducting slab to previously formed abyssal peridotites trapped within a forearc region. Abyssal peridotites representing an older lithosphere subsequently emplaced in a forearc setting may not show any evidence for their participation in partial melting in the mantle wedge (Parkinson et al. 1992; Parkinson and Pearce 1998; Pearce et al. 2000; Batanova and Sobolev 2000). The Harmancık peridotite samples have distinct whole-rock geochemical and mineral chemical compositions, suggesting their formation in several distinct stages. In the first stage, the depleted lherzolites were produced as the residues of anhydrous MOR-type melting beneath the mid-ocean ridge system within the northern branch of Neotethys. This seafloor system evolved between the Sakarya and Tauride-Anatolide continents during the early Mesozoic (Fig. 12a). Nearly 10–16 % anhydrous, decompressional partial melting of a MOR mantle beneath a cold lithospheric lid at the spreading centre formed the depleted lherzolites at this stage. The Harmancık peridotites of this stage are compositionally similar to those occurring in modern intermediate- to slow-spreading mid-ocean ridges (Uysal et al. 2007; Aldanmaz et al. 2009).

The northern branch of Neotethys started collapsing along an intra-oceanic subduction zone as early as in the mid to late Cretaceous, as the entire Tethyan realm experienced regional compression in front of the northward-moving Afro-Arabian plate (Dilek and Moores 1990; Dilek et al. 1999). The previously formed MOR oceanic lithosphere was subsequently emplaced in the upper plate of a north-dipping subduction zone (Fig. 12). In this stage, more

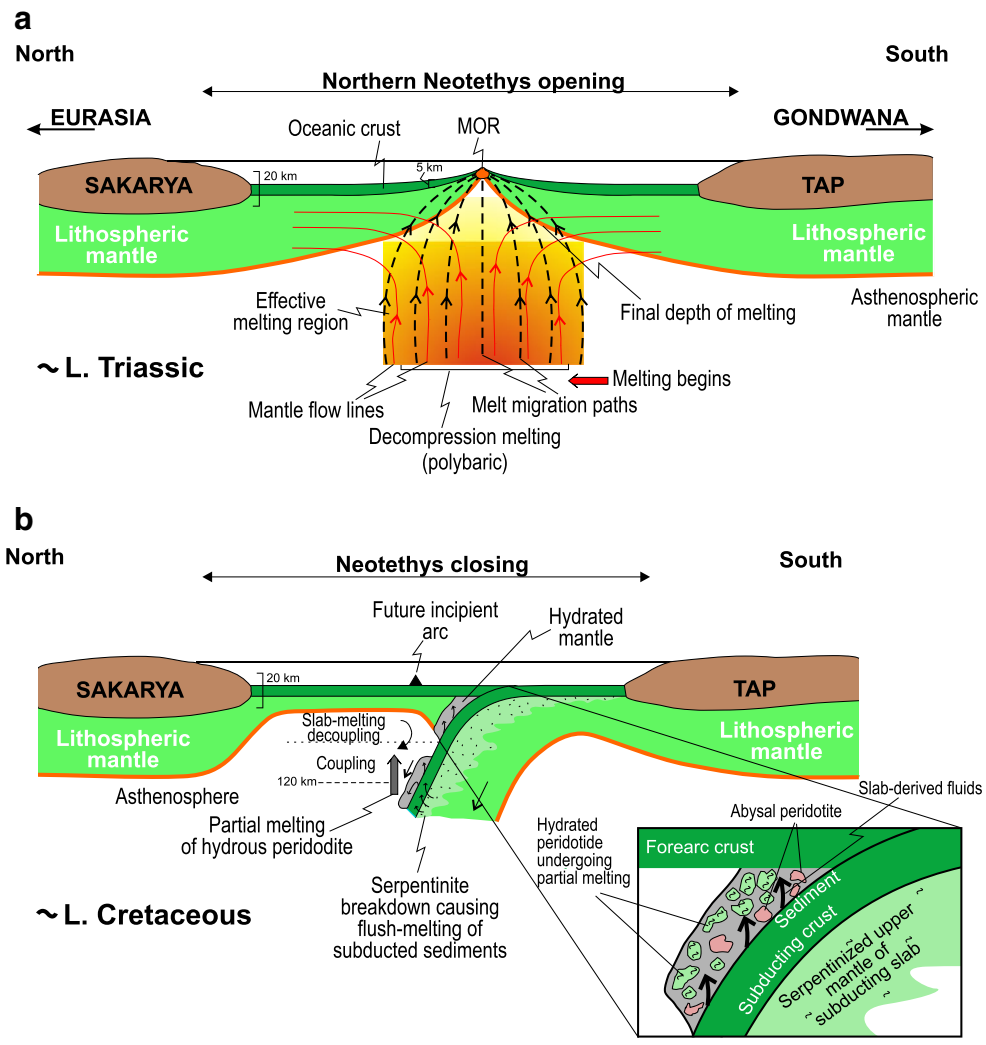

Fig. 12 Petrogenetic–tectonic model for the two-stage evolution of the Harmancık peridotites in the northern branch of Neotethys. See discussion in the text

refractory harzburgites formed as residues after ~4–11 % partial melting of a depleted MORB source (which is the residue of ~16 % partial melting of an FMM source) as a result of subduction initiated magmatism. The evidence for a supra-subduction zone origin of these harzburgites is largely based on the mineralogical and geochemical features of the samples, including the high Cr# of the spinels and the extreme low trace-element concentrations in relict pyroxenes of both the harzburgites and lherzolites. The depleted lherzolites in our study area are thus genetically related to abyssal peridotites, but they have geochemical characteristics that imply a residence time in the mantle wedge of a subduction zone during later stages of their tectonic evolution. Slab-derived fluids, particularly originated from the dehydrated serpentinites in the downgoing slab (inset in Fig. 12b) percolated through the peridotites in the mantle wedge and affected their host mantle rocks heterogeneously at all scales. Some of the abyssal peridotites trapped in this wedge were less hydrated than the surrounding mantle, largely preserving their original geochemical fingerprints (Fig. 12b).

Conclusions

The Harmancık peridotites in NW Turkey are composed of depleted lherzolites and harzburgites. Our geochemical data suggest that the depleted lherzolites representing MOR-type peridotites are residues after ~10–16 % partial melting. They resemble abyssal peridotites that are characterized by small degrees of melt extraction from a MORB source in an oceanic spreading centre. The more refractory Harmancık harzburgites, on the other hand, represent residues after ~4–11 % partial melting of a depleted (~16 % depleted) mantle source. The geochemical signatures of depleted harzburgites are typical of peridotites formed in a SSZ setting. The compositional trends between the depleted lherzolite and the more refractory harzburgite imply that melt-peridotite interaction process played a significant role during their evolution. These processes are evidenced by an increase in Cr# and TiO_2 of the spinels from the depleted lherzolites to more refractory harzburgites (Fig. 10). The geochemical compositions of the more refractory harzburgites indicate that these rocks were affected by melts in the mantle wedge. The enrichment of the LREE in the depleted harzburgite samples indicates interactions between the upper mantle rocks and subduction-derived melts and/or fluids.

Our observations from the Harmancık peridotites indicate that the upper mantle rocks exposed along the İzmir-Ankara-Erzincan suture zone in northern Turkey are not simply the products of a single melting episode during the evolution of the Mesozoic oceanic lithosphere within Northern Neotethys. Rather, they have a complex multi-stage melting history, spanning seafloor spreading and SSZ settings. Therefore, we infer that the ophiolite complexes occurring along this suture zone are also compositionally and structurally heterogeneous, composed of nested fragments of oceanic lithosphere that formed in different stages of the tectonic evolution of the northern branch of Neotethys. It should not be surprising, then, to find ophiolitic rocks with different ages (Dilek and Thy 2006), as old as the earliest Mesozoic or even older, along the İzmir-Ankara-Erzincan suture zone.

Acknowledgements Financial support of this study was provided by the project (#2008.112.005.17) of the Scientific Research Foundation of the Karadeniz Technical University (Turkey). The first author is thankful to YÖK (The Council of Higher Education of Turkey) for a post-doctoral scholarship allowing him to spend three months in Montanuniversitaet Leoben, Austria. Y Dilek acknowledges his Miami University Distinguished Professor funds in support of his global ophiolite studies. Raif Kandemir kindly helped with the preparation of some figures. We extend our special thanks to Tomoaki Morishita for his thorough review of an earlier version of this manuscript that helped us focus our thinking. Constructive reviews of an anonymous referee, Associate Editor Marco Fiorentini and Editor in Chief Johan G. Raith were insightful and are greatly appreciated.

References

Adam J, Green T (2006) Trace element partitioning between mica- and amphibole-bearing garnet lherzolite and hydrous basanitic melt: 1. Experimental results and the investigation of controls on partitioning behavior. Contrib Mineral Petrol 152:1–17

Aldanmaz E, Schmidt MW, Gourgaud A, Meisel T (2009) Mid-ocean ridge and supra-subduction geochemical signatures in spinel-peridotites from the Neotethyan ophiolites in SW Turkey: Implications for upper mantle melting processes. Lithos 113:691–708

Altunkaynak Ş, Dilek Y (2006) Timing and nature of postcollisional volcanism in western Anatolia and geodynamic implications, *in* Dilek Y, Pavlides S eds. Postcollisional tectonics and magmatism in the Mediterranean region and Asia. Geol Soc of America Spec Pap 409:321–351

Arai S (1992) Chemistry of chromian spinel in volcanic rocks as a potential guide to magma chemistry. Mineral Mag 56:173–184

Arai S (1994) Characterisation of spinel peridotites by olivine–spinel compositional relationships: review and interpretation. Chem Geol 113:191–204

Batanova VG, Sobolev AV (2000) Compositional heterogeneity in subduction-related mantle peridotites, Troodos massif, Cyprus. Geol 28:55–58

Bedard JH (1999) Petrogenesis of Boninites from the Betts Cove Ophiolite, Newfoundland, Canada: Identification of Subducted Source Components. J Petrol 40:1853–1889

Bonatti E, Michael PJ (1989) Mantle peridotites from continental rifts to ocean basins to subduction zones. Earth Planet Sci Lett 91:297–311

Burnham OM, Schweyer J (2004) Trace element analysis of geological samples by ICP-MS at the Geoscience Laboratories: revised capabilities due to improvements to instrumentation. In: Summary of Field Work and Other Activities 2004. Ontario Geological Survey Open File Report 6145, pp. 54-1–54-20.

Choi SH, Shervais JW, Mukasa SB (2008) Supra-subduction and abyssal mantle peridotites of the Coast Range ophiolite, California. Contrib Mineral Petrol 156:551–576

Dick HJB (1989) Abyssal peridotites, very slow spreading ridges and ocean ridge magmatism. In: Saunders, A. D. and Norry, M. J. (eds) Magmatism in the Ocean Basins. Geol Soc Spec Publ 42:71–105

Dick HJB, Bullen T (1984) Chromian spinel as a petrogenetic indicator in abyssal and alpine-type peridotites and spatially associated lavas. Contrib Mineral Petrol 86:54–76

Dilek Y, Altunkaynak Ş (2007) Cenozoic crustal evolution and mantle dynamics of post-collisional magmatism in western Anatolia. Int Geol Rev 49:431–453

Dilek Y, Flower MFJ (2003) Arc-trench rollback and forearc accretion: 2. A Model Template for Ophiolites in Albania, Cyprus, and Oman, *in* Dilek Y, Robinson PT eds. Ophiolites in Earth history. Geol Soc Lond Spec Publ 218:43–68

Dilek Y, Furnes H (2009) Structure and geochemistry of Tethyan ophiolites and their petrogenesis in subduction rollback systems. Lithos 113:1–20

Dilek Y, Furnes H (2011) Ophiolite genesis and global tectonics: geochemical and tectonic fingerprinting of ancient oceanic lithosphere. Geol Soc Am Bull 123:387–411

Dilek Y, Moores EM (1990) Regional tectonics of the eastern Mediterranean ophiolites. In: Malpas J, Moores E, Panayiotou A, Xenophontos C (eds) Ophiolites-Oceanic Crustal Analogues. Proceedings of Troodos Ophiolite Symposium. Geological Survey, Cyprus, pp 295–309

Dilek Y, Morishita T (2009) Melt migration and upper mantle evolution during incipient arc construction: Jurassic Eastern Mirdita ophiolite, Albania. Island Arc 18:551–554

Dilek Y, Thy P (2006) Age and petrogenesis of plagiogranite intrusions in the Ankara melange, Central Turkey. Island Arc 15:44–57

Dilek Y, Thy P (2009) Island arc tholeiite to boninitic melt evolution of the Cretaceous Kizildag (Turkey) ophiolite: Model for multi-stage early arc-forearc magmatism in Tethyan subduction factories. Lithos 113:68–87

Dilek Y, Whitney DL (1997) Counterclockwise PTt trajectory from the metamorphic sole of a Neo-Tethyan ophiolite (Turkey). Tectonophysics 280:295–301

Dilek Y, Thy P, Hacker B, Grundvig S (1999) Structure and petrology of Tauride ophiolites and mafic dike intrusions (Turkey): Implications for the Neo-Tethyan ocean. Bull Geol Soc Am 111:1192–1216

Dilek Y, Furnes H, Shallo M (2007) Suprasubduction zone ophiolite formation along the periphery of Mesozoic Gondwana. Gondwana Res 11:453–475

Droop GTR, Karakaya MÇ, Eren Y, Karakaya N (2005) Metamorphic evolution of blueschists of the Altınekin Complex, Konya area, south central Turkey. Geol J 40:127–153

Edwards SJ, Pearce JA, Freeman J (2000). New insights concerning the influence of water during the formation of podiform chromitite: In, Dilek, Y., Moores, E.M., Nicolas, A. and Elthon, D. (Eds.), Ophiolites and Oceanic Crust: New Insights from Field Studies and the Ocean Drilling Program, Geological Society of America Special Paper 349, p. 139–147.

Eiler JM, Crawford A, Elliott T, Farley KA, Valley JW, Stolper EM (2000) Oxygen isotope geochemistry of oceanic-arc lavas. J Petrol 41:229–256

Eiler JM, Schiano P, Valley JW, Kita NT, Stolper EM (2007) Oxygen-isotope and trace element constraints on the origins of silica-rich melts in the subarc mantle. Geochem Geophys Geosyst 8:Q09012

Flower MFJ, Dilek Y (2003). Arc-trench rollback and forearc accretion: 1. A collision-induced mantle flow model for Tethyan ophiolites *in* Dilek Y, Robinson PT eds. Ophiolites in Earth history: Geological Society (London) Special Publication 218:21– 41.

Gaetani GA, Grove TL (1998) The influence of water on melting of mantle peridotite. Contrib Mineral Petrol 131:323–346

Green T, Blundy JD, Adam J, Yaxley GM (2000) SIMS determination of trace element partition coefficients between garnet, clinopyroxene and hydrous basaltic liquids at 2-7.5 Gpa and 1080-1200C. Lithos 53:165–187

Hellebrand E, Snow JE, Dick HJB, Hofmann AW (2001) Coupled major and trace elements as indicators of the extent of melting in mid-ocean-ridge peridotites. Nature 410:677–681

Hellebrand E, Snow JE, Hoppe P, Hofmann AW (2002) Garnet-field melting and late-stage refertilization in residual abyssal peridotites from the Central Indian Ridge. J Petrol 43:2305–2398

Ishii T, Robinson PT, Maekawa H, Fiske R (1992). Petrological studies of peridotites from diapiric serpentinite seamounts in the Izu-Ogasawara-Mariana forearc, LEG125. *In* Proc. Ocean Drilling Project, Scientific Results (P. Fryer, J.A. Pearce and L.B. Stokking, eds.) 125:445–486.

Johnson KTM, Dick HJB (1992) Open system melting and temporal and spatial variation of peridotite and basalt at the Atlantis II Fracture Zone. J Geophys Res 97:9219–9241

Johnson KTM, Dick HJB, Shimizu N (1990) Melting in the oceanic upper mantle: An ion microprobe study of diopsides in abyssal peridotites. J Geophys Res 93:2661–2678

Kelemen PB, Hirth G, Shimizu N, Spiegelman M, Dick HJB (1997) A review of melt migration processes in the adiabatically upwelling mantle beneath oceanic spreading ridges. Philos Trans R Soc Lond 355:283–318

Kinzler RJ (1997) Melting of mantle peridotite at pressures approaching the spinel to garnet transition: Application to mid-ocean ridge basalt petrogenesis. J Geophys Res 102:853–874

Kornprobst J, Ohnenstetter D, Ohnenstetter M (1981) Na and Cr contents in cpx from peridotites: a possible discriminant between 'sub-continental' and 'sub-oceanic' mantle. Earth Planet Sci Lett 53:241–254

Manav H, Gültekin AH, Uz B (2004) Geochemical evidence for the tectonic setting of the Harmancık ophiolites, NW Turkey. J Asian Earth Sci 24:1–9

McKenzie D, O'Nions RK (1991) Partial melt distributions from inversion of rare Earth element concentrations. J Petrol 32:1021–1091

Morishita T, Tani K, Shukuno H, Harigane Y, Tamura A, Kumagai H, Hellebrand E (2011a) Diversity of melt conduits in the Izu-Bonin-Mariana forearc mantle: Implications for the earliest stage of arc magmatism. Geol 39:411–414

Morishita T, Dilek Y, Shallo M, Tamura A, Arai S (2011b) Insight into the uppermost mantle section of a maturing arc: The Eastern Mirdita ophiolite, Albania. Lithos 124:215–226

Niu Y (2004) Bulk-rock major and trace element compositions of abyssal peridotites: implications for mantle melting, melt extraction and post-melting processes beneath mid-ocean ridges. J Petrol 45:2423–2458

Niu Y, Langmuır CH, Kinzler RJ (1997) The origin of abyssal peridotites: a new perspective. Earth Planet Sci Lett 152:251–265

Ohara Y, Stern RJ, Ishii T, Yurimoto H, Yamazaki T (2002) Peridotites from the Mariana Trough: first look at the mantle beneath an active back-arc basin. Contrib Mineral Petrol 143:1–18

Okay AI (1980) Mineralogy, petrology and phase relations of glaucophane–lawsonite zone blueschists from the Tavsanlı region, Northwest Turkey. Contrib Mineral Petrol 72:243–255

Okay AI (1986). Denizli-Tavas arasındaki bölgenin jeolojisi: TPAO Arama Grubu Rap., 2042.

Okay AI, Kelley SP (1994) Tectonic setting, petrology and geochronology of jadeite+glaucophane and chloritoid+glaucophane schists from northwest Turkey. J Metamorph Geol 12:455–466

Ozawa K, Shimuzi N (1995) Open-system melting in the upper mantle: Constraints from the Hayachine-Miyamori ophiolite, northeastern Japan. J Geophys Res 100:22315–22335

Özkoçak O (1969). Etude geologique du massif ultrabasique D'Orhaneli et de sa Proche bordure (Bursa-Turquie). Unpublished PhD Thesis, University of Paris.

Palme H, O'Neill HSC (2004) Cosmochemical estimates of Mantle Composition. In: Holland HD, Turrekian KK (eds) Treatise on Geochem. vol 2. Elsevier, Amsterdam, pp 1–38, Cosmochemical estimates of Mantle Composition

Parkinson IJ, Pearce JA (1998) Peridotites from the Izu–Bonin–Mariana forearc (ODP Leg 125): evidence for mantle melting and melt–mantle interaction in a suprasubduction zone setting. J Petrol 39:1577–1618

Parkinson IJ, Pearce JA, Thirlwall MF, Johnson KTM, Ingram G (1992) Trace element geochemistry of peridotites from the Izu–Bonin–Mariana forearc, Leg 125. In: Fryer P, Pearce JA, Stokking LB et al (eds) Proceedings of the Ocean Drilling Program Scientific Results, 125. College Station, TX, Ocean Drilling Program, pp 487–506

Parkinson IJ, Arculus RJ, Eggins SM (2003) Peridotite xenoliths from Grenada, Lesser Antilles Island Arcs. Contrib Mineral Petrol 146:241–262

Parlak O, Höck V, Delaloye M (2002) The supra-subduction zone Pozanti-Karsanti ophiolite, Southern Turkey: evidence for high-pressure crystal fractionation of ultramafic cumulates. Lithos 65:205–224

Pearce JA, Robinson PT (2010) The Troodos ophiolitic complex probably formed in a subduction initiation, slab edge setting. Gondwana Res 18:60–81

Pearce JA, Harris NBW, Tindle AG (1984) Trace element discrimination diagrams for the tectonic interpretation of granitic rocks. J Petrol 25:956–983

Pearce JA, van der Laan SR, Arculus RJ, Murton BJ, Ishii T, Peate DW, Parkinson IJ (1992) Boninite and Harzburgite from Leg 125 (Bonin-Mariana Forearc): A Case Study of Magma Genesis during the Initial Stages of Subduction. Proc Ocean Drill Program Sci Results 125:623–659

Pearce JA, Barker PF, Edwards SJ, Parkinson IJ, Leat PT (2000) Geochemical and tectonic significance of peridotites from the South Sandwich arc-basin system, South Atlantic. Contrib Mineral Petrol 139:36–53

Piccardo GB, Zanetti A, Müntener O (2007) Melt/peridotite interaction in the Southern Lanzo peridotite: Field, textural and geochemical evidence. Lithos 94:181–209

Rampone E, Piccardo GB, Hofmann AW (2008) Multi-stage melt-rock interaction in the Mt. Maggiore (Corsica, France) ophiolitic peridotites: microstructural and geochemical evidence. Contrib Mineral Petrol 156:453–475

Robertson AHF (1994) Role of the tectonic facies concept in orogenic analysis and its application to Tethys in the Eastern Mediterranean region. Earth Sci Rev 37:139–213

Rolland Y, Billo S, Corsini M, Sosson M, Galoyan G (2009) Blueschists of the Amassia-Stepanavan Suture Zone (Armenia): linking Tethys subduction history from E-Turkey to W-Iran. Int J Earth Sci (Geol Rundsch) 98:533–550

Seyler M, Lorand JP, Dick HJB, Drouin M (2007) Pervasive melt percolation reactions in ultra-depleted refractory harzburgites at the Mid-Atlantic Ridge, 15–20 N: ODP Hole 1274A. Contrib Mineral Petrol 153:303–319

Sherlock S, Kelley S, Inger S, Harris N, Okay AI (1999) ^{40}Ar–^{39}Ar and Rb–Sr geochronology of high-pressure metamorphism and exhumation history of the Tavşanlı Zone, NW Turkey. Contrib Mineral Petrol 137:46–58

Suhr G (1999) Melt migration under oceanic ridges: Inferences from reactive transport modelling of upper mantle hosted dunites. J Petrol 40:575–599

Tankut A, Dilek Y, Önen P (1998) Petrology and geochemistry of the Neo-Tethyan volcanism as revealed in the Ankara Melange, Turkey. J Volcanol Geotherm Res 85:265–284

Topuz G, Okay AI, Altherr R, Meyer HP, Nasdala L (2006) Partial high-pressure aragonitization of micritic limestones in an accretionary complex, Tavşanlı Zone, NW Turkey. J Metamorph Geol 24:603–613

Uysal I, Kaliwoda M, Karsli O, Tarkian M, Sadiklar MB, Ottley CJ (2007) Compositional variations as a result of partial melting and melt-peridotite interaction in an upper mantle section from the Ortaca area, southwestern Turkey. Can Mineral 45:1471–1493

Uysal I, Ersoy EY, Karsli O, Dilek Y, Sadiklar MB, Ottley CJ, Tiepolo M, Meisel T (2012) Coexistence of abyssal and ultra-depleted SSZ type mantle peridotites in a Neo-Tethyan Ophiolite in SW Turkey: Constraints from mineral composition, whole-rock geochemistry (major–trace–REE–PGE), and Re–Os isotope systematics. Lithos 132–133:50–69

Zhou MF, Robinson P (1997) Origin and tectonic environment of podiform chromite deposits. Econ Geol 92:259–262

Zou HB (1998) Trace element fractionation during modal and nonmodal dynamic melting and open-system melting: A mathematical treatment. Geochim Cosmochim Acta 62:1937–1945